Engineering method to estimate the blade loading of propellers in nonuniform flow

van Arnhem, Nando; de Vries, Reynard; Sinnige, Tomas; Vos, Roelof; Eitelberg, Georg; Veldhuis, Leo L.M.

DOI
10.2514/1.J059485

Publication date
2020

Document Version
Final published version

Published in
AIAA Journal

AIAA JOURNAL
Vol. 58, No. 12, December 2020

Engineering Method to Estimate the Blade Loading of Propellers in Nonuniform Flow

Nando van Arnhem,* Reynard de Vries,† Tomas Sinnige,‡ Roelof Vos,§ Georg Eitelberg,¶ and Leo L. M. Veldhuis¶
Delft University of Technology, 2629 HS Delft, The Netherlands

https://doi.org/10.2514/1.J059485

Advances in aerodynamic and propulsive efficiency of future aircraft can be achieved by strategic installation of propellers near the airframe. This paper presents a robust and computationally efficient engineering method to estimate the load distribution of a propeller operating in arbitrary nonuniform flow that is induced by the airframe and by different flight conditions. The time-resolved loading distribution is computed by determining the local blade section advance ratio and using the sensitivity distribution along the blade, which is a property of the propeller in isolated conditions. The method is applied to four representative validation cases by comparing to full-blade computational fluid dynamics (CFD) simulations and experimental data. For the evaluated cases, it is shown that the changes in the propeller loads due to the nonuniform inflow are predicted with errors ranging from 0.5 up to 12% compared to the validation data. By extending the quasi-steady approach with a correction to account for unsteady effects, the time-resolved blade loading is also well approximated, without adding computational cost. The proposed method provided a time-resolved solution within several central processing unit seconds, which is seven orders of magnitude faster compared to full-blade CFD computations.

Nomenclature

B	=	number of blades
C_m	=	pitching moment coefficient; $m/\rho_\infty n^2 D_\mathrm{p}^5$
C_n	=	yawing moment coefficient; $n/\rho_\infty n^2 D_\mathrm{p}^5$
C_{p_t}	=	total pressure coefficient; $(p_\mathrm{t} - p_{\mathrm{t}_\infty}/q_\infty) + 1$
C_Q	=	torque coefficient; $Q/\rho_\infty n^2 D_\mathrm{p}^5$
C'_Q	=	section torque coefficient; $Q'/\rho_\infty n^2 D_\mathrm{p}^5$, m^{-1}
C_T	=	thrust coefficient; $T/\rho_\infty n^2 D_\mathrm{p}^4$
C'_T	=	section thrust coefficient; $T'/\rho_\infty n^2 D_\mathrm{p}^4$, m^{-1}
C_Y	=	in-plane force coefficient; $F_Y/\rho_\infty n^2 D_\mathrm{p}^4$
C_Z	=	in-plane force coefficient; $F_Z/\rho_\infty n^2 D_\mathrm{p}^4$
c	=	chord, m
D	=	diameter, m
F	=	force, N
h_i	=	average cell size of grid i, m
J	=	advance ratio; V/nD_p
k	=	wave number, m^{-1}
M	=	Mach number
m	=	pitching moment, N/m
N	=	normal force, N
n	=	rotational speed, s^{-1}; and yawing moment, N/m
P_s	=	shaft power, W
p	=	pressure, Pa; and observed order of accuracy
Q	=	torque, N/m
Q'	=	sectional torque, N
q	=	dynamic pressure, Pa
R	=	radius, m
r	=	radial coordinate, m
S	=	area, m^2; and Sears function
T	=	thrust, N
T_C	=	thrust coefficient; $T/q_\infty S_\mathrm{p}$
T'	=	sectional thrust, m^{-1}
U_s	=	standard deviation based on observed order
U_ϕ	=	estimated discretization uncertainty
u, v, w	=	velocity in Cartesian system, m $\cdot$ s^{-1}
V	=	velocity, m $\cdot$ s^{-1}
x, y, z	=	Cartesian coordinates, m
α	=	angle of attack, deg
β	=	blade-pitch angle, deg
Γ	=	circulation, s^{-1}
ϵ	=	propeller tip clearance, m
ζ	=	compressibility factor; $\sqrt{1-M^2}$
η	=	efficiency
ρ	=	density, kg/m^{-3}
σ	=	reduced frequency; $knc/4\pi V$
ϕ	=	propeller phase angle, deg

Subscripts

a	=	axial component
B	=	blade component
eff	=	effective
h	=	hub
p	=	propeller
t	=	tangential component
us, qs	=	unsteady and quasi steady
∞	=	freestream quantity

Superscripts

$'$	=	local quantity at r/R_p
*	=	based on theoretical order of convergence

Received 19 February 2020; revision received 11 June 2020; accepted for publication 14 June 2020; published online 6 October 2020.

*Ph.D. Candidate, Flight Performance and Propulsion Section, Faculty of Aerospace Engineering; N.vanArnhem@tudelft.nl. Member AIAA.
†Ph.D. Candidate, Flight Performance and Propulsion Section, Faculty of Aerospace Engineering. Member AIAA.
‡Assistant Professor, Flight Performance and Propulsion Section, Faculty of Aerospace Engineering. Member AIAA.
§Assistant Professor, Flight Performance and Propulsion Section, Faculty of Aerospace Engineering. Associate Fellow AIAA.
¶Full Professor, Flight Performance and Propulsion Section, Faculty of Aerospace Engineering. Member AIAA.

I. Introduction

PROPELLERS are an attractive means of aircraft propulsion for low to moderate flight Mach numbers because of their inherent high efficiency [1–4]. The choice for a particular propeller location relative to the airframe can be motivated by several design criteria, for example, structural rigidity of the engine mounting, weight and balance, and ground clearance constraints [1]. For numerous existing

and proposed configurations, the propeller installation is carefully chosen with the objective to gain an overall aircraft performance benefit by increasing the propeller efficiency, airframe performance, and/or reducing the noise footprint [1,5]. Examples include wingtip-mounted propellers [6–11], over-the-wing propellers [12–16], boundary-layer ingestion configurations [17,18], and leading-edge distributed propellers [19]. Additionally, enhancements of the aeropropulsive efficiency that can be reached by distributing the propulsion along the airframe also make the utilization of (hybrid-)electric propulsion more feasible [20]. The installation of propellers in the vicinity of the airframe leads to an aerodynamic interaction: the propeller alters the airframe forces by inducing a pressure and velocity field, whereas the airframe induces a flowfield that affects the propeller forces. Figure 1 depicts a number of typical cases of nonuniform inflow, either caused by the airframe-induced flow or the flight condition, such as an angle of attack. Depending on the configuration, the disturbances of the inflow can range from concentrated perturbations to a more distributed nonuniformity over the propeller disk. From the examples illustrated by Fig. 1, it can be deduced that for a typical application, there is (without exception) a disturbed inflow to the propeller that will vary between flight conditions; and it will affect the propeller forces and moments.

In a general sense, an arbitrary time-averaged inflow to the propeller disk can be characterized as a combination of out-of-plane and in-plane momentum transport. The perturbation to the freestream velocity field $\Delta \boldsymbol{V}$ can be decomposed into a change in advance ratio $\Delta J(r, \phi)$ such that at each radial location and phase angle, the effective advance ratio becomes $J_{\text{eff}}(r, \phi) = J_\infty + \Delta J(r, \phi)$. If the nominal operating condition is in the nearly linear region of the C_T–J curve, a reduction in the local effective advance ratio locally results in a higher thrust, higher torque, and higher thrust-to-power ratio [21]. An azimuthal variation in the advance ratio has a number of consequences. First, the propeller rotation makes the loads on the blade periodic, typically leading to additional noise [2,22,23], fatigue loads on the blades, and vibrations to the airframe [24]. Second, in-plane forces and moments are generated [25], which alter the trim condition and stability characteristics of the aircraft: in particular, for propellers at a relatively large distance to the aircraft's center of gravity [1,26–28]. Finally, the propulsive efficiency of the propeller can be positively or negatively affected.

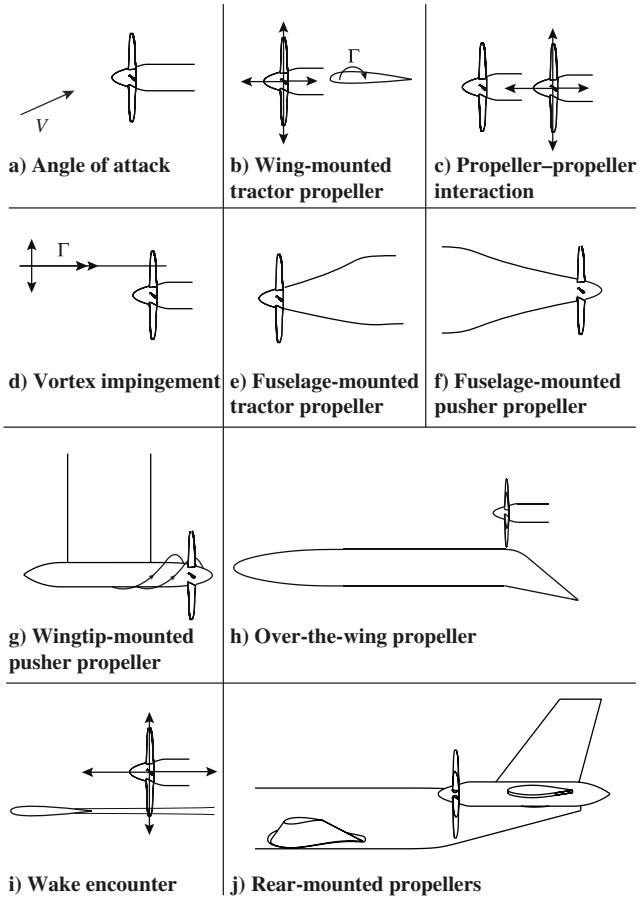

Fig. 1 Typical cases of propellers experiencing nonuniform inflow.

The extent to which the propeller performance is altered by the installation depends on the type and magnitude of the nonuniform inflow, the propeller operating condition, and the propeller design. For example, local disturbances, such as the propeller encountering a wake or vortex, have a negligible to a small effect on the mean propeller forces; whereas they do cause significant unsteady loads and noise [29–35]. Asymmetric inflow, such as a propeller at a nonzero angle of attack or a propeller operating in the upwash or downwash of a wing, only changes the propeller performance slightly but still leads to significant unsteady loads and nonnegligible in-plane forces [24,36–42]. Moreover, quasi-axisymmetric inflows covering a large part of the propeller disk, such as a swirling inflow to a wingtip-mounted pusher-propeller or a boundary-layer inflow, have shown to alter the propeller efficiency [6,43–45]. If the combined performance of the airframe and propeller is to be assessed over a range of flight conditions, understanding and quantifying the effect of the inflow is essential: in particular, for configurations featuring highly integrated propellers. For those configurations, an estimation of aircraft performance based on propeller data for isolated conditions is insufficient.

Next to a range of prediction methods for axisymmetric inflow [46–48], several authors have published works on load prediction and analyses of propellers in nonuniform inflow, by employing experimental, numerical, and analytical methods. Changing the geometry in an experimental setup is often laborious, and therefore experimental methods are often not suitable for design studies. Furthermore, deducing the propeller blade loading from a flowfield measured at some distance downstream of the installed propeller is not straightforward: in particular, when the slipstream is distorted due to interactions with the airframe [3,49–52]. Despite the introduced modeling errors, an analytical or numerical prediction of the installed propeller performance may be preferred instead: in particular, if relatively small performance changes are expected.

A number of analytical expressions for the in-plane forces for an isolated propeller at an angle of attack have been formulated, of which the formulas by de Young [25,53] are widely used. These formulas were adapted in Refs. [28,54] to account for the induced inflow by the fuselage and wing for wing-mounted tractor propellers. However, a generic nonuniform inflow can rarely be reduced to an equivalent angle of attack, which makes such analytical expressions less suitable for nonuniform inflows that only influence part of the propeller disk.

Numerical methods are therefore often preferred because the actual constitution of nonuniform inflow can be taken into account. In coupled approaches, the flow solution of the combined airframe and propeller is solved directly. These include unsteady Reynolds-averaged Navier–Stokes (RANS) computational fluid dynamics (CFD) methods [55] and panel methods [56] with a full representation of the propeller blade. Such approaches are particularly useful if the propeller has a strong effect on the airframe. If one is primarily interested in the propeller performance, the additional accuracy may not outweigh the additional computational cost and effort to analyze a full configuration, as compared to a superposition of the individual contributions of the propeller–airframe interaction. If the nonuniformity of the inflow is dominated by the isolated airframe, one can argue that the dominant changes in propeller loading due to the interaction are already captured if the inflow is treated as being decoupled. However, even with this simplification, the cost can still be significant if the full propeller is modeled. On the other hand, lower-order models are generally not able to account for nonaxisymmetric flows and may lack the fidelity to capture the relevant flow phenomena: in particular, for more complex blade geometries featuring, for example, blade sweep.

In this paper, a computationally efficient method is presented to determine the response of propeller forces and moments due to an arbitrary nonuniform flow, based on blade-loading distributions in uninstalled conditions and an inflow field. A prediction of these loads is useful in both the preliminary and the detailed design phases

because it can assist aircraft designers to select appropriate locations of the propeller along the airframe in a multidisciplinary design synthesis, for example, to improve the time-averaged performance of the propeller or to reduce unsteady loads. An efficient prediction method of the load distribution can also be used to provide inputs in noise studies [53,57,58] or provide inputs for actuator disk and actuator line models to assess propeller–airframe aerodynamic interaction [55].

The engineering method is presented in Sec. II. In Sec. III, a validation study is presented on a reference propeller in uniform flow, along with the characterization of the propeller performance that is used as input to the engineering method. The predicted load distributions and integral propeller performance in case of nonuniform inflow are then compared with validation data for four representative reference cases in Sec. IV.

II. Description of the Method

The engineering method initially assumes that the propeller response to a nonuniform inflow is a quasi-steady problem. The solution is later improved by applying a correction to account for unsteady effects.

A. Quasi-Steady Solution Method

The method proposed in this paper to estimate propeller blade loading treats the nonuniformity of the inflow field induced by the airframe and flight condition (i.e., the inflow at the propeller plane that exists in absence of the propeller) as a local disturbance to the nominal operating condition. The main principle of the method is that it is assumed that a change in local advance ratio $\Delta J'$ at r/R_p results in a local change in load, C_T', and C_Q', and therefore the induced velocity field, with a magnitude equal to the one that would be obtained if $\Delta J'$ is applied to the full propeller disk as $\Delta J = \Delta J'$. The prime indicates a local quantity at a determined location on the propeller disk, given by its azimuthal and radial position. This principle is schematically shown in Fig. 2.

This underlying assumption is based on three principles. First, it is implicitly assumed that the local sensitivity of a section at r/R_p to a disturbance is determined by the nominal load distribution that exists in uniform inflow conditions. The analogy can be made to a three-dimensional wing, for which the local slope of the lift curve along the span is proportional to its nominal lift distribution. It is shown in Sec. III.E that for a propeller blade, the normalized thrust distribution is nearly independent of the advance ratio; hence, the sensitivity to a change in advance ratio is also proportional to the nominal load distribution. Second, since a perturbation of the inflow leads to a variation of the bound circulation relative to the one obtained in uniform inflow, the associated shed vorticity induces an upwash/downwash to adjacent sections. It is assumed that the redistribution of loading along the radius is a second-order effect. Since thrust and torque are dominated by the lift force and induced drag on a blade section, the response to a nonuniform inflow for a propeller is analogous to the resulting changes in lift and drag due to a perturbation distributed along the span of a wing. It is shown in Supplemental Data S1 that the error of the estimation of the integral forces by neglecting this redistribution indeed becomes a second-order effect if the spanwise gradient of the perturbation is small. A similar approach is used in blade-element momentum models, where the direct influence of adjacent blade sections is also neglected in the computation of local blade forces and only a tip-loss factor is applied along the blade. Finally, the blade–blade mutual interference as a consequence of the perturbation in loading is proven in Ref. [59] to be an effect of several orders of magnitude smaller than the primary change in load due to the perturbation if the average spacing between blades is several chord lengths. Therefore, it is assumed for the quasi-steady solution that a blade response to a disturbance is confined to the same azimuthal angle at which the disturbance is encountered by a blade. The propeller–airframe interaction is therefore linearized; i.e., the perturbations $\Delta u, \Delta v, \Delta w$ at the location of the propeller disk are the ones that exist in absence of the propeller. In this way, a computationally intensive analysis of the full annulus is avoided.

For the computation of the quasi-steady load distribution, both the propeller performance (that is, the radial load distribution for a range of advance ratios) of the isolated propeller in uniform flow and the propeller inflow field ($\boldsymbol{V}$ and ρ, respectively) are assumed to be known in advance. These quantities can be obtained by various analysis methods.

The propeller blade is described as a line, spanning from hub to tip, sweeping through an arbitrary flowfield, as depicted in Fig. 3. Along this line, the local inflow at location (r, ϕ) is used to compute the local forces and moments. The temporal resolution of the estimated solution depends on the spatial resolution of this flowfield.

In the presented approach, the propeller load distribution is treated as a linear superposition of the response to in-plane disturbances $\Delta v, \Delta w$ and out-of-plane disturbance Δu. This superposition is permissible when the perturbations are small. By treating the in-plane and out-of-plane disturbances separately, insight is gained on their relative contribution. Moreover, the response of the propeller to a change in tangential or axial inflow is different. At a given rotational speed n, the disk loading varies approximately *linearly* with a change in *axial* velocity because $C_T - J$ is approximately linear and J is linear with V:

$$\frac{T}{S_p} = \frac{4}{\pi}\rho D_p^2 n^2 C_T, \quad \text{where } C_T \propto J \tag{1}$$

Similarly, at no change in axial velocity but an inflow constituted of tangential velocity components, the disk loading varies *quadratically* with a *tangential* inflow velocity V_t because the T_C–J curve is hyperbolic:

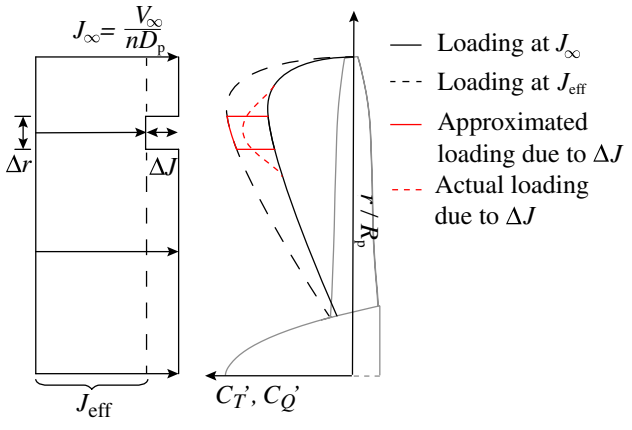

Fig. 2 Illustration of relation between local effective advance ratio and change in blade loading.

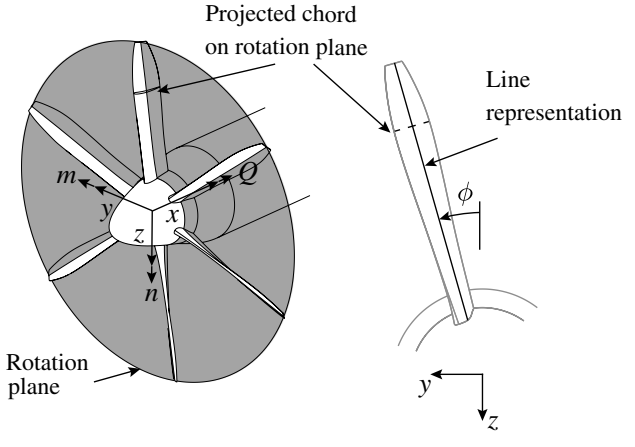

Fig. 3 Definition of the propeller rotation plane on which the inflow is determined.

$$\frac{T}{S_\mathrm{p}} = \frac{1}{2}\rho V^2 T_C, \quad \text{where } T_C \propto \frac{1}{J} \tag{2}$$

Therefore, for a propeller operating at a given condition (i.e., V_∞ and n), the thrust and torque are more sensitive to a change in advance ratio caused by V_t than V_a at moderate- to high-thrust conditions, demonstrated in Sec. III.E. At high advance ratios (i.e., near windmilling conditions), the trend is reversed; instead, the blade sections are more sensitive to a change in V_a than V_t. Therefore, the inflow disturbance needs to be associated with the corresponding sensitivity. Since the radial distribution of thrust, $C'_T(r, J_\infty)$, and torque, $C'_Q(r, J_\infty)$, are known for the isolated propeller, these need to be evaluated at the local, effective advance ratio determined by the nonuniform inflow. This distinction is made such that $J_{\mathrm{eff}_\mathrm{a}}$ is the effective advance ratio due to *axial inflow*, whereas $J_{\mathrm{eff}_\mathrm{t}}$ is the effective advance ratio only due to *tangential inflow*. At constant rotational speed, the effective advance ratio due to axial inflow is

$$J_{\mathrm{eff}_\mathrm{a}}(r,\phi) = \frac{\Delta u(r,\phi)}{nD_\mathrm{p}} + \frac{V_\infty}{nD_\mathrm{p}} \tag{3}$$

Only the tangential components of the in-plane velocities Δv and Δw are of interest, and they are decomposed into a tangential velocity using the local phase angle ϕ:

$$\Delta V_\mathrm{t} = -\Delta v \cos\phi - \Delta w \sin\phi \tag{4}$$

which yields an effective advance ratio of

$$J_{\mathrm{eff}_\mathrm{t}}(r,\phi) = \frac{V_\infty}{[n + (\Delta V_\mathrm{t}/2\pi r)]D_\mathrm{p}} - \frac{V_\infty}{nD_\mathrm{p}} \tag{5}$$

For the uniform inflow case, it follows that $J_{\mathrm{eff}_\mathrm{t}} = 0$ and $J_{\mathrm{eff}_\mathrm{a}} = J_\infty$. If $C'_T(J_\mathrm{eff})$ is the local section thrust coefficient on a blade operating in *uniform inflow* at the corresponding effective advance ratio J_eff, the corresponding changes in local thrust and torque due to $\Delta J_{\mathrm{eff}_\mathrm{a}}$ are

$$T'_\mathrm{a}(r,\phi) = \left[C'_T(J_{\mathrm{eff}_\mathrm{a}})\frac{\rho}{\rho_\infty} - C'_T(J_\infty)\right]\rho_\infty n^2 D_p^4 \tag{6}$$

$$Q'_\mathrm{a}(r,\phi) = \left[C'_Q(J_{\mathrm{eff}_\mathrm{a}})\frac{\rho}{\rho_\infty} - C'_Q(J_\infty)\right]\rho_\infty n^2 D_p^5 \tag{7}$$

Equivalently, the change in thrust due to an in-plane disturbance $J_{\mathrm{eff}_\mathrm{t}}$ is

$$\Delta T'_\mathrm{t}(r,\phi) = \left[C'_T(J_{\mathrm{eff}_\mathrm{t}})\cdot\left(n + \frac{\Delta V_\mathrm{t}}{2\pi r}\right)^2\frac{\rho}{\rho_\infty} - C'_T(J_\infty)n^2\right]\rho_\infty D_\mathrm{p}^4 \tag{8}$$

$$\Delta Q'_\mathrm{t}(r,\phi) = \left[C'_Q(J_{\mathrm{eff}_\mathrm{t}})\cdot\left(n + \frac{\Delta V_\mathrm{t}}{2\pi r}\right)^2\frac{\rho}{\rho_\infty} - C'_Q(J_\infty)n^2\right]\rho_\infty D_\mathrm{p}^5 \tag{9}$$

To determine the thrust and torque expressed by Eqs. (6–9), one needs to compute or measure $C'_T(r, J)$ and $C'_Q(r, J)$ for a range of advance ratios of the propeller in isolated conditions, of which an example is shown in Sec. III.E. Furthermore, one needs to determine the flowfield in which the propeller is operating.

The summation of the in-plane and out-of-plane contributions yields the total change in normalized propeller loading at a particular blade section position (r, ϕ):

$$\Delta C'_T(r,\phi) = \frac{\Delta T'_\mathrm{a} + \Delta T'_\mathrm{t}}{\rho_\infty n^2 D_\mathrm{p}^4} \tag{10}$$

$$\Delta C'_Q(r,\phi) = \frac{\Delta Q'_\mathrm{a} + \Delta Q'_\mathrm{t}}{\rho_\infty n^2 D_\mathrm{p}^5} \tag{11}$$

Once the load distribution is found by evaluating Eqs. (3–11) at each phase angle, the integral propeller forces are computed by integration:

$$\Delta C_T = \frac{1}{2\pi}\int_0^{2\pi}\int_{R_\mathrm{h}}^{R_\mathrm{p}} \Delta C'_T(r,\phi)\,\mathrm{d}r\,\mathrm{d}\phi \tag{12}$$

$$\Delta C_Y = -\frac{1}{2\pi}\int_0^{2\pi}\int_{R_\mathrm{h}}^{R_\mathrm{p}} \frac{\Delta C'_Q(r,\phi)}{r}\cos\phi\,\mathrm{d}r\,\mathrm{d}\phi \tag{13}$$

$$\Delta C_Z = -\frac{1}{2\pi}\int_0^{2\pi}\int_{R_\mathrm{h}}^{R_\mathrm{p}} \frac{\Delta C'_Q(r,\phi)}{r}\sin\phi\,\mathrm{d}r\,\mathrm{d}\phi \tag{14}$$

and the integral propeller moments become

$$\Delta C_Q = \frac{1}{2\pi}\int_0^{2\pi}\int_{R_\mathrm{h}}^{R_\mathrm{p}} \Delta C'_Q(r,\phi)\,\mathrm{d}r\,\mathrm{d}\phi \tag{15}$$

$$\Delta C_n = -\frac{1}{2\pi D_p}\int_0^{2\pi}\int_{R_\mathrm{h}}^{R_\mathrm{p}} \Delta C'_T(r,\phi) r\sin\phi\,\mathrm{d}r\,\mathrm{d}\phi \tag{16}$$

$$\Delta C_m = -\frac{1}{2\pi D_\mathrm{p}}\int_0^{2\pi}\int_{R_\mathrm{h}}^{R_\mathrm{p}} \Delta C'_T(r,\phi) r\cos\phi\,\mathrm{d}r\,\mathrm{d}\phi \tag{17}$$

The change in power coefficient follows from Eq. (15) as $\Delta C_P = 2\pi\Delta C_Q$. Conventionally, the efficiency is defined as the ratio of useful work done on the fluid per unit time to the power that is put into the system to perform the useful work. Although the propeller is doing work on a fluid having a velocity of $\boldsymbol{V} = (u, v, w)$, which is generally not equal to V_∞, one is only interested in the change of the thrust-to-power ratio of the propeller at the flight speed of the vehicle. Therefore, the efficiency of a propeller in close proximity of the airframe with a nonuniform inflow is determined in a straightforward way by using the computed thrust and torque:

$$\Delta\eta_\mathrm{p} = \frac{(\Delta T + T_\infty)}{(\Delta P_\mathrm{s} + P_{\mathrm{s}_\infty})}V_\infty - \frac{T_\infty}{P_{\mathrm{s}_\infty}}V_\infty \tag{18}$$

The treatment of the local response to a nonuniformity of the inflow is, in particular, suitable for unswept propeller blades because a high sweep angle leads to a more pronounced coupling between adjacent sections along the radius. Furthermore, the evaluation of inflow along the line assumes the chord length is effectively zero. However, as observed in Ref. [30], the forces on the blade sections are particularly influenced by the flow conditions around the propeller leading edge, analogous to the sensitivity to a change in angle of attack of the load distribution along the chord for typical two-dimensional airfoils [60]. Hence, an improved representation of the inflow can be obtained when the inflow at location (r, ϕ) is determined by a weighted velocity along the projected chord in the plane of rotation.

B. Accounting for Unsteady Effects

The response of a two-dimensional airfoil to a change in inflow is not instantaneous. As explained by Sears [61], a downwash is induced at the leading edge by the bound vorticity and wake vorticity. This not only reduces the section lift coefficient but also introduces a difference in phase between unsteady motion of the inflow and the response to the disturbance. By accounting for these unsteady effects, the temporal response of the blade forces, and therefore the relative importance of the resulting in-plane loads, is predicted more accurately compared to the quasi-steady solution. The utilization of the Sears function is a well accepted approach to determine the transient lift response of a two-dimensional airfoil to a gust [35,62,63]. The response of the introduced induced drag and the change in profile drag of the two-dimensional airfoil can be determined using the approach of Ref. [64], and it is comparable to the lift response. However, the application of a separate correction on lift and drag would require an estimation of the local induced velocity to obtain the local velocity vector to decompose

lift and drag. As the thrust and torque forces on a section are typically dominated by the lift force, instead, a straightforward approach is used here. In this paper, the radial load distributions of thrust and torque are corrected by directly applying Sears's function. The quasi-steady forces of Eqs. (6–9) are transformed to the frequency domain and are multiplied with Sears's function:

$$T'_{us}(r,\sigma) = T'_{qs}(r,\sigma)S(r,\sigma) \tag{19}$$

and

$$\frac{Q'_{us}(r,\sigma)}{r} = \frac{Q'_{qs}(r,\sigma)}{r}S(r,\sigma) \tag{20}$$

with σ being the reduced frequency $\sigma = (k\Omega c/2V)$, and S being the Sears function. V is the magnitude of the local helicoidal inflow velocity to a section in the nominal, isolated conditions, and therefore includes the induced velocity. In case the induced velocities are unknown, the actuator disk theory could be used as a first-order estimate. The Sears function for incompressible flow $S_{M=0}$ is defined by Ref. [61] as

$$\begin{aligned} S_{M=0}(\sigma) &= [J_0(\sigma) - iJ_1(\sigma)]C(\sigma) + iJ_1(\sigma) \\ &= \frac{J_0(\sigma)K_1(i\sigma) + iJ_1(\sigma)K_0(i\sigma)}{K_1(i\sigma) + K_0(i\sigma)} \end{aligned} \tag{21}$$

with C as Theodorsen's function, J_0 and J_1 as the zeroth- and first-order Bessel functions of the first kind, and K_0 and K_1 the modified zeroth- and first-order Bessel functions of the second kind. A compressibility correction in line with Ref. [62] is applied to account for compressibility effects, which are typically not negligible on outboard sections. Reference [62] applies a compressibility correction on both the lift-curve slope and the reduced frequency. As the predicted quasi-steady loads already include the effect of compressibility on the section forces through the analysis of the isolated propeller, only the reduced frequency is corrected:

$$S(\sigma,M) = S_{M=0}(\sigma/\zeta^2)\left\{J_0\left(\frac{M^2\sigma}{\zeta^2}\right) + \mathrm{i}J_1\left(\frac{M^2\sigma}{\zeta^2}\right)\right\}\mathrm{e}^{[-i\sigma f(M)/\zeta^2]} \tag{22}$$

with M as the effective Mach number, ζ as the Prandtl–Glauert compressibility factor based on the effective Mach number, and f as a correction factor defined by

$$f(M) = (1-\zeta)\,\ell_n(M) + \zeta\,\ell_n(1+\zeta) - \ell_n(2) \tag{23}$$

Equation (22) is valid for $\sigma M/\zeta^2 < 1$ [62]. For the considered cases in Sec. IV, this condition is met. The unsteady response over a full revolution in the time domain is computed by taking the inverse Fourier transform of the product of the quasi-steady loading and the Sears function: Eqs. (19) and (20).

III. Validation and Characterization of Propeller Performance in Uniform Inflow

The method presented in Sec. II requires the performance characteristics $C'_T(r,J)$ and $C'_Q(r,J)$ of the propeller operating in uniform flow. These are quantified in this section for a reference propeller by means of RANS CFD simulations. The results of these simulations are also compared to experimental data to determine the validity of the load distributions. The computed performance characteristics are subsequently used in the validation study in Sec. IV.

A. Propeller Geometry

The propeller that was selected for this study, referred to as XPROP-S, has a representative load distribution that is close to minimum induced loss for nominal operating conditions. The blade geometry is a scaled version of the geometry used in Ref. [65]. The propeller has a diameter of 0.2032 m, and its six blades are set to a blade-pitch angle of 45 deg at 70% of the radius. The choice for the high blade pitch was made to achieve high thrust and torque coefficients at relatively high advance ratios, representative of cruise conditions of a full-scale aircraft [27]. The propeller features a Clark-Y airfoil family, and the sections have a minimum trailing-edge thickness of 0.2 mm due to manufacturing constraints. As the blade sections are stacked on approximately the centerline of the blade, there is a minor forward–backward sweep of the quarter-chord line from hub to tip. The propeller and spinner are attached to a circular nacelle. A technical drawing and propeller blade-pitch and chord distributions are provided in Fig. 4, which also shows the simplifications made in the CFD model. The corresponding CAD geometries are attached to this paper as Supplemental Data S2.

B. Computational Setup

The performance of the isolated propeller was simulated numerically by solving the RANS equations for compressible flow using ANSYS® Fluent Release 18.1 [66], which is a commercial, unstructured, finite volume, and cell-centered solver. The isolated propeller was solved in the wedge-shaped domain depicted in Fig. 5, consisting of subdomains with refined grids. At the nominal condition of the isolated propeller ($J = 1.8$), no time dependency of the solution is found; therefore, a multireference frame approach is used that reduces the problem to steady simulations. The propeller blades, spinner, and nacelle are modeled as no-slip walls; whereas the nacelle was a moving wall. Periodic conditions are used on the sides of the wedge, whereas the total pressure and total temperature are specified on the inlet, which are equal to the conditions of the experimental campaign (Sec. III.C.1) at $V_\infty = 40$ m/s. The mean static pressure on the outlet was set to ambient conditions. A Riemann invariant pressure far-field condition

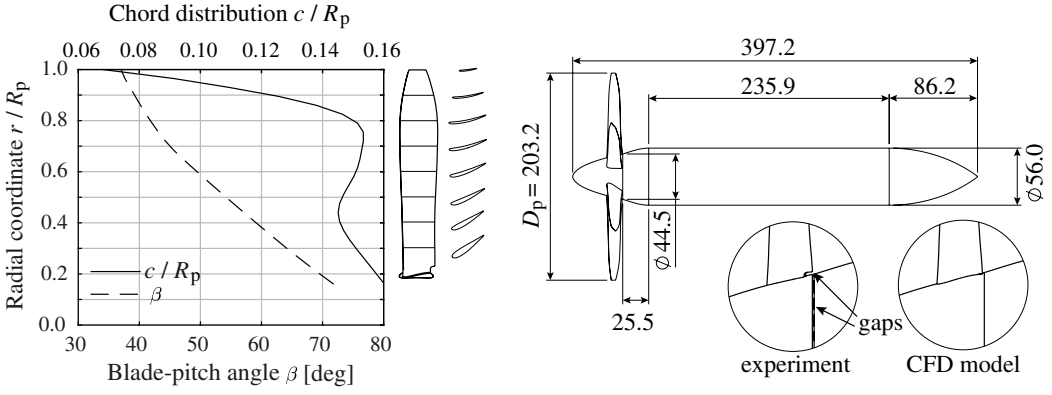

a) Pitch and chord distribution

b) Main dimensions of propeller and nacelle (dimensions in millimeters)

Fig. 4 XPROP-S propeller and nacelle geometries.

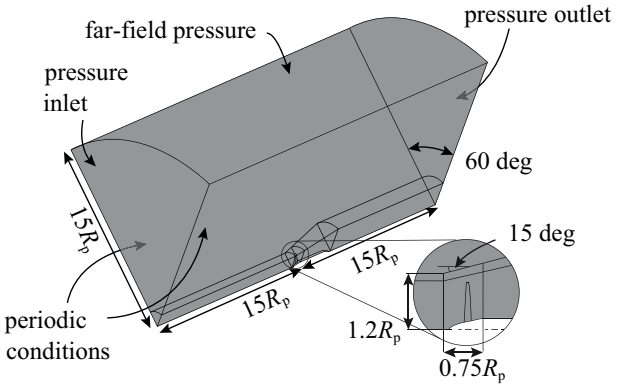

Fig. 5 Computational domain and boundary conditions for the simulations of the isolated propeller.

is specified on the remaining boundary, with a Mach number, static pressure, and static temperature complying with the inlet conditions. The size of the domain was selected such that the proximity of the boundaries does not influence the solution, which is verified by the assessment of the gradients of flow quantities in the radial, upstream, and downstream directions. The mesh contains tetrahedral elements, with 28 prism layers from the walls. A growth rate of 1.2 is selected throughout the domain.

A second-order upwind spatial discretization is employed using a coupled pressure–velocity scheme. The flow is prescribed to be fully turbulent, and the Spalart–Allmaras turbulence model with the strain/vorticity-based production equation is applied to solve the closure of the RANS equations, which was shown to compare well with experiments of propeller–wing simulations with similar Reynolds numbers in Refs. [27,55]. A maximum y^+ of one is obtained, resulting in a resolved boundary layer. Values for the inlet turbulence quantities are based on the recommendations by Spalart and Rumsey [67]. Standard sea-level atmospheric conditions are used for the freestream flow; for the equation of state, an ideal gas is assumed; and Sutherland's law is applied to predict the corresponding dynamic viscosity.

Table 1 Different grids for the isolated propeller simulations

Grid	h_i/h_1	Number of elements
1	1.00	17,986,198
2	1.25	9,163,007
3	1.55	4,841,676
4	1.87	2,744,493

To quantify the discretization error of several performance indicators, four meshes with different refinements are analyzed. The refinements are systematically varied with a refinement factor of 1.3 applied to volume and surface refinements, whereas the inflation layer is kept approximately constant. This leads to the mean refinement factors for the complete domain as listed in Table 1. A least-squares version of the grid convergence index as proposed by Eça and Hoekstra [68] is applied to estimate the discretization error, in a similar manner as the study done in Ref. [55]. As follows from Fig. 6b, the finest grid shows a slightly larger total pressure gradient in the tip-vortex region: the result of less diffusion with the finer mesh in the slipstream. The distribution shows a low dependency on the different grids over the majority of the radius, whereas a significant reduction in the peak-to-peak total pressure is observed in the tip vortex, which is in line with the results of, e.g., Ref. [55]. Only minor differences are observable when the phase-averaged total pressure distributions are compared up to $r/R_p = 0.8$ in Fig. 6c. The grid convergence of the maximum rise in total pressure, shown in Fig. 6c, displays a diverging trend toward the finer grids. However, a fit of second order still leads to good fit with a small fitting error U_s^*. Similarly, the distribution of local thrust in Table 2 shows an oscillatory convergence, whereas a second-order fit still yields acceptable values of the standard deviation and estimated discretization error for grid 3. Despite the different order of the best-fitting curve to the thrust and power coefficients (Figs. 6e and 6f, respectively), the second-order fit is considered appropriate to estimate the discretization error at $h_i/h_1 = 0$ due to the low standard deviation as shown in Table 2. For the integral thrust and power of the propeller, this error is within 1% for grid 3. Therefore, grid 3 is selected as a compromise between computational efficiency and

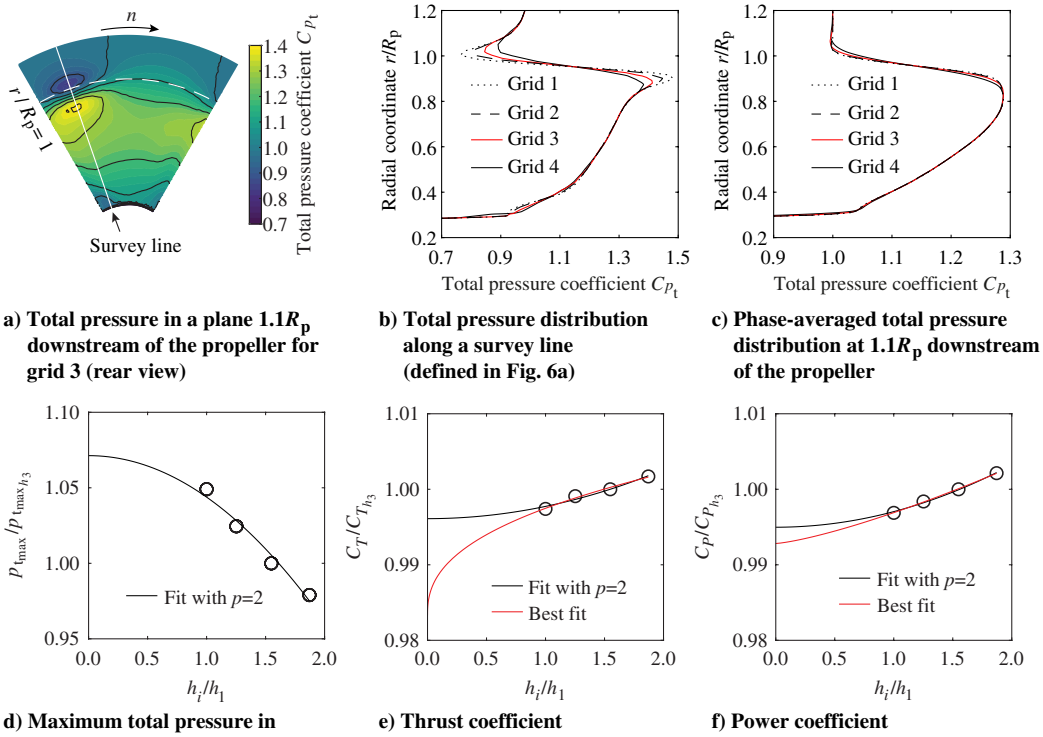

a) Total pressure in a plane $1.1R_p$ downstream of the propeller for grid 3 (rear view)

b) Total pressure distribution along a survey line (defined in Fig. 6a)

c) Phase-averaged total pressure distribution at $1.1R_p$ downstream of the propeller

d) Maximum total pressure in slipstream

e) Thrust coefficient

f) Power coefficient

Fig. 6 Mesh refinement study for the isolated propeller grids.

Table 2 Results of grid study for the isolated propeller: values are based on grid 3

	C_T	C_P	$\max(p_t)$	$(T')_{0.85R_p}$	$(Q')_{0.85R_p}$
p	0.40	1.31	— —	— —	— —
U_s, %	0.04	0.01	— —	— —	— —
U_s^*, %	0.06	0.03	0.92	0.17	0.07
$\lvert U_s \rvert$, %	0.55	0.91	9.83	0.68	0.24

accuracy because the finer grids only lead to marginal differences in propeller slipstream quantities and integral forces. For this grid, 40% of the elements are located in the propeller blade domain and 37% in the domain of the slipstream. The patch conforming blade surface mesh has 69 cells on each side in the chordwise direction and 154 cells in the radial direction.

C. Experimental Setup

1. *Model, Facility, and Test Conditions*

The experimental campaign of the isolated propeller was performed at the Delft University of Technology in the Low-turbulence tunnel, which is a closed-return low-speed wind tunnel. The nacelle was mounted on a support strut with a NACA0030 airfoil profile that was connected to a six-component external balance. The velocity field at the propeller plane that is induced by the support is estimated to be on the order of 0.1% of the freestream velocity, for which no corrections are applied. Transition of the boundary layer was enforced on the nacelle and support (Fig. 7a), whereas no transition was applied on the stainless steel propeller blades. The model was installed in an octagonal test section, with its dimensions indicated in Supplemental Data S2.

The nacelle housed an electric motor that was driven by an electronic speed controller and a power supply. An in-house-developed control system controlled the motor rotational speed to a set point that could be set with a precision of 0.01 Hz. Maximum fluctuations of 0.1 Hz were registered around the set point, as registered by means of a rotary optical encoder mounted on the motor shaft.

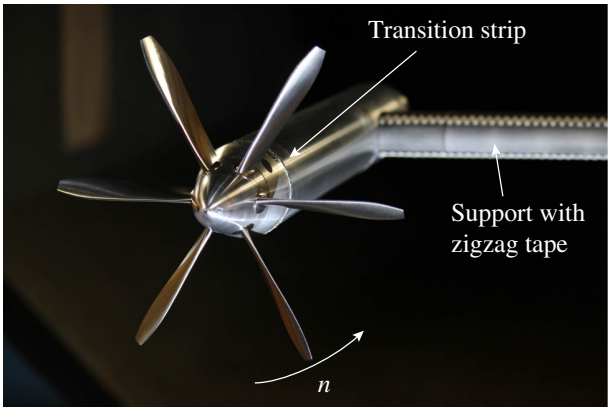

a) Propeller model

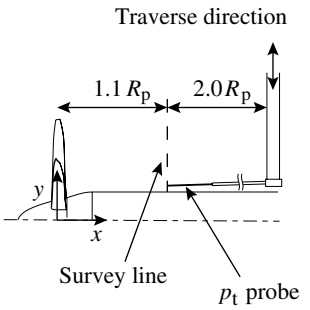

b) Pitot probe

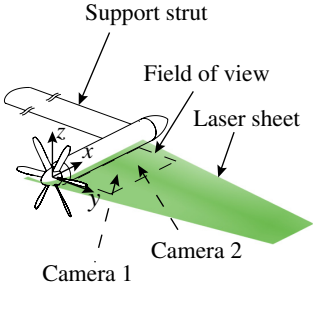

c) Stereoscopic PIV

Fig. 7 Isolated propeller installed on a support in low turbulence tunnel at Delft University of Technology and the setups to measure the slipstream of the isolated propeller.

Table 3 Measurement and processing characteristics of the PIV setup

Parameter	Value
Cameras	2 × 6 megapixel sCMOS
Focal length	105 mm
Laser	200 mJ Nd:YAG
Field of view	260 × 100 mm
Pulse separation	14 μs
Image resolution	19 pixels/mm
Interrogation window size	24 pixels^2
Window overlap	50%
Uncertainty mean velocity magnitude	$0.025V_\infty$

sCMOS = scientific complementary metal–oxide–semiconductor.
Nd:YAG = Neodymium-doped Yttrium Aluminum Garnet.

A freestream velocity of 40 m/s was selected as the baseline condition, and it was based on the operational limits of the electric motor. At this velocity, the turbulence level was below 0.1%. Both propeller-off and propeller-on measurements were performed, where the advance ratio was varied from $J = 2.3$ to $J = 1.6$ by varying the rotational speed of the propeller, achieving thrust coefficients between $T_C = 0.01$ and $T_C = 0.28$.

2. *Measurement Techniques and Uncertainty*

The propeller–support model was attached to a six-component external balance for integral thrust measurements averaged over an acquisition time of 20 s for each condition. Tare measurements were taken with the same setup using a nonrotating dummy spinner. No correction was applied to account for the aerodynamic interaction of the propeller slipstream with the nacelle and support strut. For the range of aerodynamic forces measured in this experiment, the six-component external balance has an uncertainty of 0.002 to 0.01 N, depending on the force component. The blade-pitch angle could be set with an accuracy of ±0.05 deg, and its associated uncertainty in propeller load distribution was determined using the CFD model of the isolated propeller; and it is included in the error bars of the flowfield measurements. Only a thrust-dependent correction in line with Ref. [69] for slipstream blockage was applied to the experimental data to obtain the equivalent advance ratio to compare with the numerical model, which does not include wind-tunnel walls.

The total pressure and static pressure far upstream of the model were measured over 5 s per measurement point using an electronic pressure scanner having a measurement uncertainty of ±4 Pa. For validation purposes, total pressure measurements were taken using a pitot probe connected to the same pressure scanner at a survey line of $1.1R_p$ downstream of the plane of rotation, as sketched in Fig. 7b. Although the local flow is not aligned with the total pressure probe, in Ref. [70], it was found that angles up to 20 deg yield a total pressure with a maximum error of 1% for a pitot tube with an internally conical-shaped tip. This condition was met in the majority of the slipstream, except in the tip-vortex region, where the measured total pressure should be interpreted with care.

The velocity field in the slipstream was measured by means of stereoscopic particle image velocimetry (PIV) [71] in a plane aligned with the propeller rotation axis, which is schematically shown in Fig. 7c. Phase-averaged measurements were performed by acquiring 500 image pairs at arbitrary phase angles. Also, phase-locked measurements were performed using a one-per-revolution trigger signal from the rotary encoder, and they are used to compare the velocity field of individual tip-vortex and wake structures, which was constructed by averaging 300 image pairs. Table 3 lists further details of the PIV setup.

D. Validation of Computational Setup

Figure 8a shows the C_T–J curve computed by CFD (obtained by integrating the pressure and viscous forces on the blade) and the experimentally obtained values for a range of freestream velocities. Similar to the findings by Bass [72], there is a clear influence of the Reynolds number on C_T, with a significant shift in the C_T curve at $V_\infty = 20$ m/s compared to 50 m/s. With respect to the measured

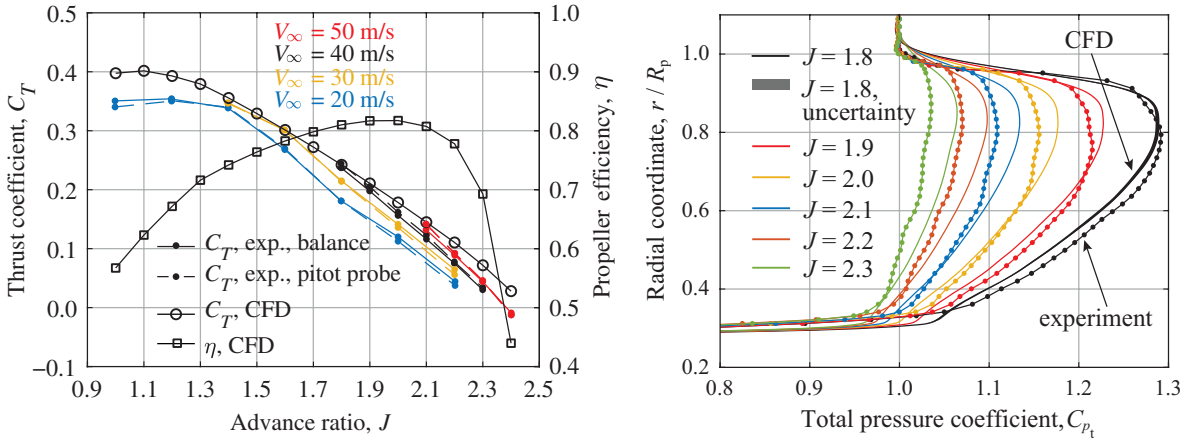

a) Propeller performance

b) Time-averaged total pressure distribution downstream of the propeller at V_∞ = 40 m/s

Fig. 8 Propeller thrust and flowfield obtained in the experiment (exp.) and computed using CFD at $\alpha = 0$ deg.

data, the computed curves show an offset and a lower slope. For these conditions, the range of Reynolds number based on propeller chord at $r/R_p = 0.7$ varies between 30,000 and 80,000. Simulation with a two-dimensional viscous–inviscid coupled panel code indicates a significant dependency of the aerodynamic properties of the highly cambered airfoils on the Reynolds number (not shown in this paper). The flow is expected to be predominately laminar in the experiment. Compared to a laminar solution, the fully turbulent boundary layer results in a reduction of the slope of the airfoil lift curve, due to the decambering of the boundary layer, and a shift of the airfoil lift curve, reflected as a difference in slope and an offset of the C_T–J curve. As shown in Ref. [73], a more pronounced crossflow exists in the leading-edge region at low advance ratios, which could lead to a crossflow instability and earlier transition on the blade in the experiment than would occur due to Tollmien–Schlichting instability. At a high advance ratio, there is a relatively strong crossflow in the boundary layer toward the trailing edge of the blade. Since, at high advance ratios, the relative contribution of viscous forces is large, the relative error between CFD and the experiment is also more pronounced. Vice versa, at low advance ratios, the pressure forces dominate and the inaccuracy in the contribution of the viscous forces is reduced; hence, a better agreement between CFD and the experiment can be expected at low advance ratios, as shown in Fig. 8a.

A better insight into these deviations can be obtained by comparing the total pressure profile in the slipstream (Fig. 8b) measured at $1.1R_p$ behind the propeller. The profiles show a slightly irregular loading distribution at high advance ratios at a radial location with highest loading, which is expected to be the result of laminar separation. At lower advance ratios, the waviness in the loading distributions disappears and the numerically computed total pressure distribution approaches the measured distribution. From the figure, it becomes clear that the contraction of the slipstream is slightly underestimated by the numerical simulations, similar to the results in, e.g., Ref. [55]. Note that the shaded region around the computed C_{p_t} at $J = 1.8$ indicates the uncertainty in the slipstream distribution due to uncertainty in the blade-pitch angle and fluctuations in rotational speed in the experiment, and is shown to be negligible.

The time-averaged velocity fields in Fig. 9 are representative for comparison of the load distributions between CFD and the experiment, as these entail the added momentum in along the radius.

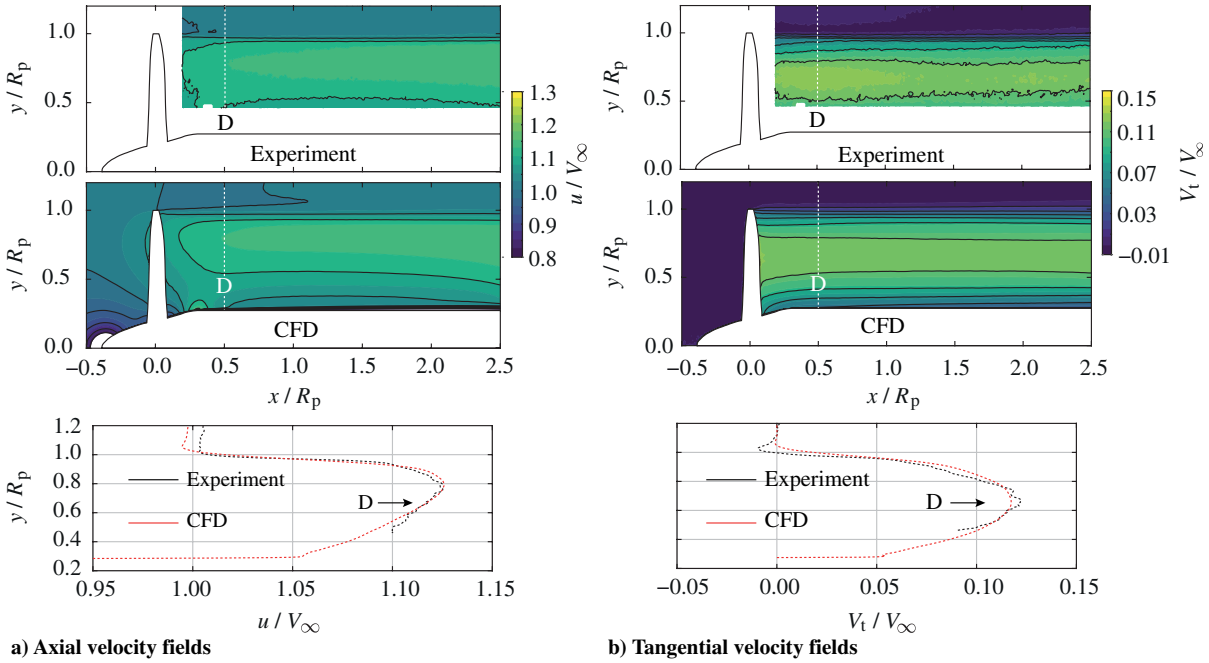

a) Axial velocity fields

b) Tangential velocity fields

Fig. 9 Comparison of the time-averaged propeller slipstream at $J = 1.8$, measured by means of stereoscopic PIV and computed by full-blade CFD.

The good agreement of the phase-averaged profiles of the swirl and axial velocity at $0.5R_p$ downstream of the propeller plane indicates that the computed thrust and torque distributions are close to the ones in the experiment. For the interested reader, in Supplemental Data S3, the phase-locked PIV is compared with the CFD results. Those figures show a lower-velocity gradient through the vortex in the computed velocity field, which is comparable to the findings in Ref. [55] and is the result of a more diffused tip vortex. As the loading distribution is the primary focus of this study, the slipstream development far downstream and the local gradients in velocity are of secondary importance. It is therefore concluded that the validity of the CFD model of the isolated propeller is sufficient and serves the purpose of this study to use its loading distributions in subsequent analyses. The measured flowfields for $J = 1.8$, $J = 2.0$, and propeller-off conditions can be found in Supplemental Data S4.

E. Load Distributions as Input to Method

The load distributions of the propeller in uniform flow are required as input for the engineering method, as was discussed in Sec. II. These distributions are obtained by evaluating the propeller in uniform flow for a range of advance ratios to construct a response surface on which Eqs. (7–9) are interpolated. The distributions are attached to this paper as Supplemental Data S5.

Figure 10a shows the thrust distribution along the radius, normalized with the integral thrust of the propeller, and has a maximum around $r/R_p = 0.8$ to 0.9, which is typical for a minimum induced loss propeller [21]. The figure also indicates that the normalized shape is practically independent of advance ratio. This behavior has a distinct advantage: If the radial distribution is known at a single advance ratio, as well as the slope of the C_T–J curve at that condition, the radial distribution at an advance ratio within the linear range of the C_T–J curve can be constructed, without the need to analyze a large number

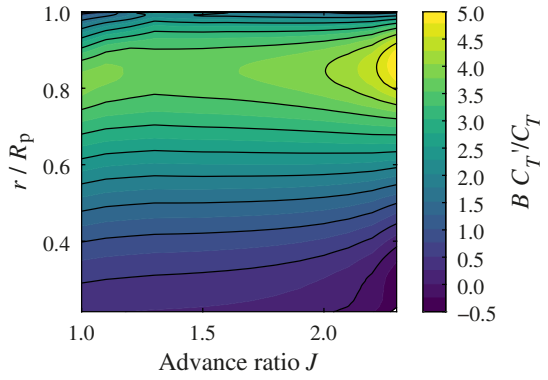

a) Normalized radial thrust coefficient

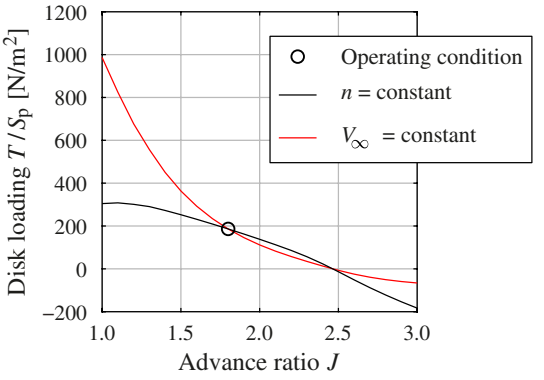

b) Disk loading by varying n or varying V

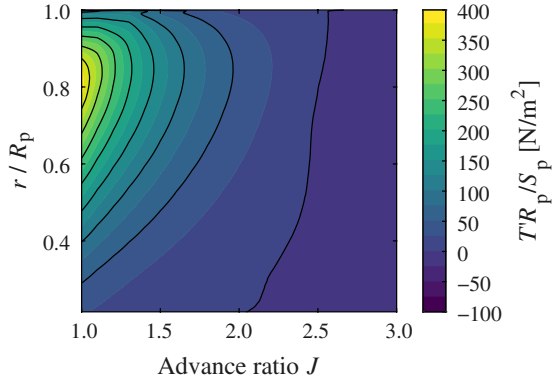

c) Distribution of sectional disk loading with V = 40 m/s (constant)

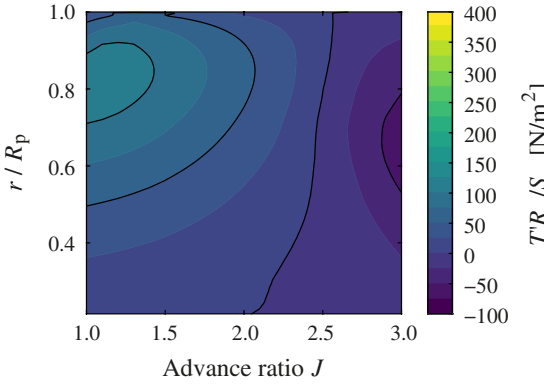

d) Distribution of sectional disk loading with n = 109.4 Hz (constant)

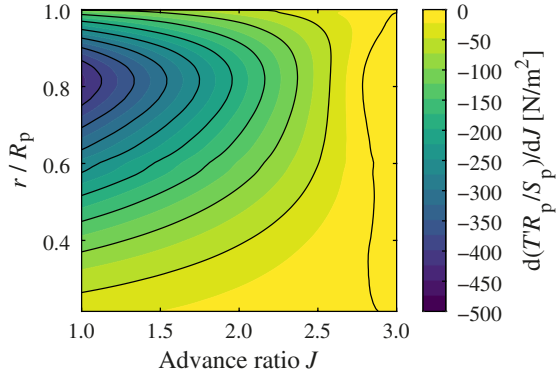

e) Derivative of sectional disk loading with respect to J (constructed from Fig. 10c)

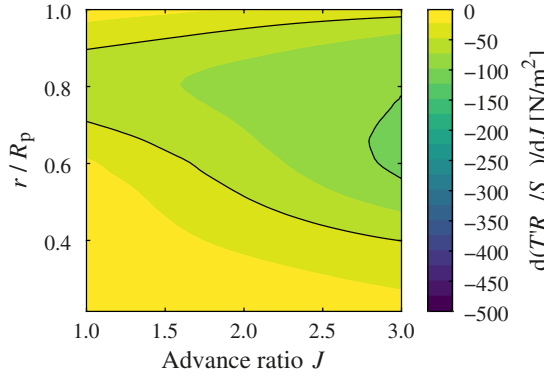

f) Derivative of sectional disk loading with respect to J (constructed from Fig. 10d)

Fig.10 Computed radial distributions of the XPROP-S that are used as input to the method.

of conditions. The actual distributions for the full range of advance ratios are used throughout this paper because they include the nonlinear region ($J < 1.3$).

In Sec. II, a distinction was made between tangential and axial inflow to determine the change in thrust and torque. Figure 10b clearly illustrates the motivation for this distinction. When, at a uniform inflow condition, the axial velocity is varied, the disk loading varies along the black curve, whereas a change in rotational speed is described by the quadratic red curve. Effectively, if the advance ratio is increased due to a swirling inflow, the change in thrust is larger than when the same change in advance ratio is obtained by a different axial inflow velocity at constant rotational speed. The characteristic of a different sensitivity around the nominal condition is well observable in the thrust distribution along the blade, by comparing Figs. 10c and 10d. The contours depicting the derivative of the thrust with respect to the advance ratio (Figs. 10e and 10f) also reveal that the region of highest loading (i.e., $r/R_p = 0.8$) is most sensitive to a change in advance ratio. Figure 10d is obtained by first applying a manipulation to account for a constant rotational speed around the nominal condition

$$C'_{T_{n=\text{constant}}} = C'_{T_{V=\text{constant}}} \left(\frac{n}{n_{\text{nominal}}} \right)^2 \tag{24}$$

IV. Validation of the Method

A. Definition of Validation Cases and the Inflow Fields as Input to Method

The method is validated by comparing the load distributions, integral blade loads, and integral propeller forces with unsteady RANS simulations and experimental data of four representative validation cases that feature a range of different types of inflow, summarized in Table 4. Part of the validation data is generated by performing unsteady CFD simulations of the XPROP-S, using a sliding-mesh approach [66] with a time step equal to 2 deg of propeller rotation with 35 inner iterations, and using a second-order implicit temporal discretization. For consistency, the domains containing the propeller and nacelle in the transient simulations are a copy of those domains that are used for the analyses of the isolated propeller. For each of the four validation cases, the inflow fields are evaluated at the plane of the propeller and are summarized in Fig. 11.

An in-plane nonuniformity that is distributed over the propeller disk is simulated by providing an angle of attack (case 1; Fig. 1a) to the XPROP-S propeller. Figure 11a depicts the change in effective advance ratio and shows that the dominating component is the result of the in-plane velocity field, leading to changes in the effective advance ratio of up to 35% of the freestream value, with a minimum at $\phi = 90$ deg and a maximum at $\phi = 270$ deg. The axial induced velocity by the nacelle introduces only a slight asymmetry in the inflow.

A concentrated disturbance is simulated by generating a wake that enters the propeller disk at different vertical locations (case 2; Fig. 1i). The viscous wake trailed from a straight, untapered, and untwisted wing that was situated upstream of the XPROP-S propeller. The corresponding dimensions, computational domain, and boundary conditions are presented in Ref. [74]. For a wing that is situated at $z/R_p = 0.5$, the change in advance ratios is depicted in Fig. 11b, showing a maximum reduction of $\Delta J_a = 0.27$ caused by a maximum velocity defect of $0.15V_\infty$. As the in-plane induced flowfield downstream of the wing is negligible, the tangential velocity is nearly zero, and therefore $\Delta J_t \approx 0$.

A flowfield consisting of both in-plane and out-of-plane flow was generated by mounting the XPROP-S propeller above a wing with a plain flap (case 3; Fig. 1h). The predicted integral thrust as function of tip clearance is compared to experimental data from de Vries et al. [16]. The inflow to the propeller was obtained by simulating the wing section in a domain including wind-tunnel walls but excluding the support strut. To gain confidence that the simulated inflow field is close to the one in the experiment, the measured and computed pressure distributions are compared in Supplemental Data S6. The propeller experiences a strong variation of ΔJ_a over the disk, depicted in Fig. 11c, caused by the variation of axial velocity at the propeller location from $0.1V_\infty$ to $0.3V_\infty$. The in-plane velocity due to the wing circulation and curvature also varies over the propeller disk and is observed by the propeller as a negative angle of attack.

A combination of a distributed and concentrated nonuniform inflow is generated by mounting a pusher propeller to the tip of a wing (case 4; Fig. 1g) such that the propeller encounters both a swirling inflow (due to the wingtip vortex) as well as a wing wake. The mesh and inflow distributions from Stokkermans et al. [44] were used to obtain the required validation data. A similar propeller as XPROP-S was used, which has approximately the same blade geometry, a blade pitch of $\beta_{0.7R_p} = 30$ deg and a diameter of 0.4064 m. The performance maps discussed in Sec. III.E were separately quantified for this

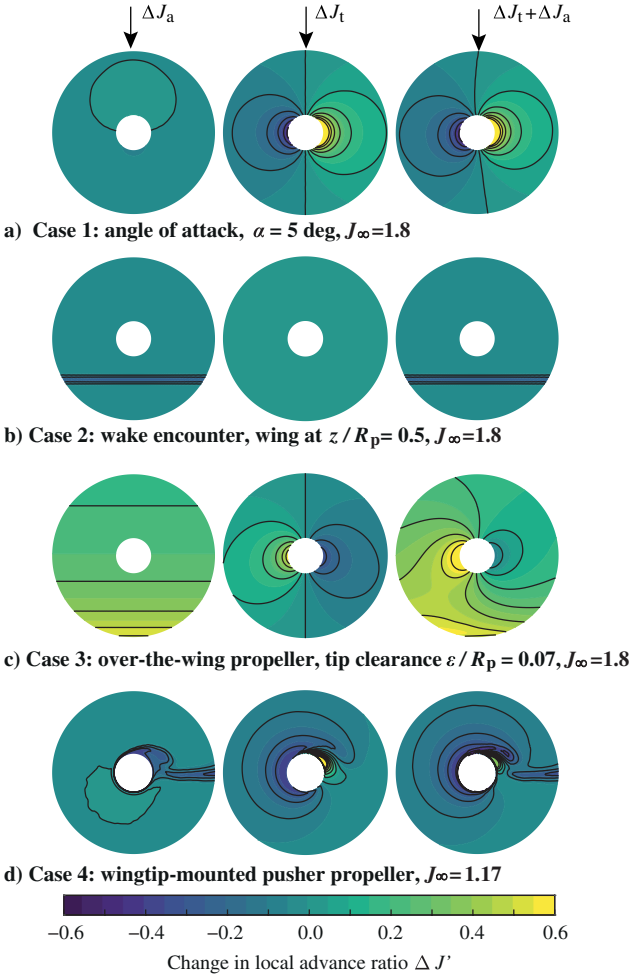

Fig. 11 Computed inflow profiles of the four validation cases that are used as input to the method.

Table 4 Characteristics of the validation cases indicated by check mark

	Validation case no.			
	1	2	3	4
In- plane disturbance ΔJ_t	✓	— —	✓	✓
Out-of-plane disturbance ΔJ_a	✓	✓	✓	✓
Vortical inflow	— —	— —	— —	✓
Defect in total pressure	— —	✓	— —	✓
Local disturbance	— —	✓	— —	✓
Disturbance over full disk	✓	— —	✓	✓
Small propeller–airframe separation	— —	— —	✓	✓
Large propeller–airframe separation	— —	✓	— —	— —

propeller (not shown in this paper). Figure 11d shows a highly nonaxisymmetric inflow caused by the swirling flow induced by the wingtip, the wing downwash, and the viscous wing wake. The axial induced flow is driven by the viscous wake and the junction flow between the nacelle and wing surface. Although the wingtip and propeller axis are aligned, the wingtip vortex rolls over the nacelle, causing a large variation of J_t.

B. Validation of the Propeller Blade Loads

In this section, the predicted propeller forces by the method are compared to unsteady CFD simulations and experimental data. Figure 12 depicts the predicted change of integral blade thrust, torque, side force, and normal force coefficients over a full revolution compared to the ones that were computed by the full-blade CFD simulations. For the propeller at an angle of attack (case 1), the blade loads are nearly sinusoidal, with a period of one per revolution for the thrust and torque and a period of two per revolution for the in-plane forces. The quasi-steady method underpredicts the peak-to-peak load and introduces a phase advance with respect to the full-blade simulations. The maximum change in advance ratio occurs at $\phi = 90$ deg and $\phi = 270$ deg (Fig. 11a), whereas the maximum change in load occurs with approximately a 15 deg lag in the full-blade CFD results, which is in line with findings in Refs. [36,38]. This delay is accurately captured by applying the unsteady correction to the quasi-steady result, and it indicates that it can be predominantly attributed to the response of the two-dimensional blade sections that experience an unsteady inflow. This behavior is also clearly visible by comparing the $C_{T'}$ distribution over the disk in Fig. 13a and is approximately constant along the blade. As the predicted load distribution has a phase advance, the relative values of the integral in-plane forces (depicted in Fig. 14a) are inaccurate; in particular, the predicted C_Y shows a relatively large deviation. The nonzero C_Y from the quasi-steady solution is attributed to the difference in thrust at $\phi = 0$ deg and $\phi = 180$ deg due to the nacelle induced axial velocity field. By using the unsteady correction, the C_Y–α curve is closer to the full-blade CFD result. The strong variation of loading over the disk for this case results in a significantly nonuniform propeller slipstream and leads to an increase of the force magnitude in the full-blade simulation. As the actual slipstream is not computed, the predicted quasi-steady loads are too low; and these are further reduced by the application of the unsteady correction model. Despite the fact that the root mean square of the blade thrust is underpredicted by 12 and 24% by the quasi-steady and unsteady methods, the integral thrust and torque nearly coincide with the full-blade simulation. It is noted that the integral thrust and torque are not affected by the application of the Sears function over a full revolution and the quasi-steady and unsteady result are identical, as can be deduced from Eq. (21).

For case 2, the predicted evolutions of integral blade forces compare well with the full-blade CFD simulation in terms of magnitude and phase, shown in Fig. 12b. The transient after the steep rise and fall of the load is inherently not captured by the quasi-steady approach, but it is shown to be quite well predicted when the Sears function is applied. It is worth noting that the character of the blade force over a revolution is highly dependent on the location at which the wake is encountered. The fact that two distinct peaks are present when the wing is at $z/R_p = 0.5$ is attributed to the more sensitive response to a change in advance ratio in the highest loaded region of the blade, as shown in Fig. 10.

This difference in sensitivity is also clearly observable as the two distinct regions on the propeller disk with higher forces in Fig. 13b. If the wake is encountered toward the tip, the two peaks in Fig. 12b merge into a single peak. From Fig. 13b, it also follows that even though in the full-blade simulation the load is slightly more smeared

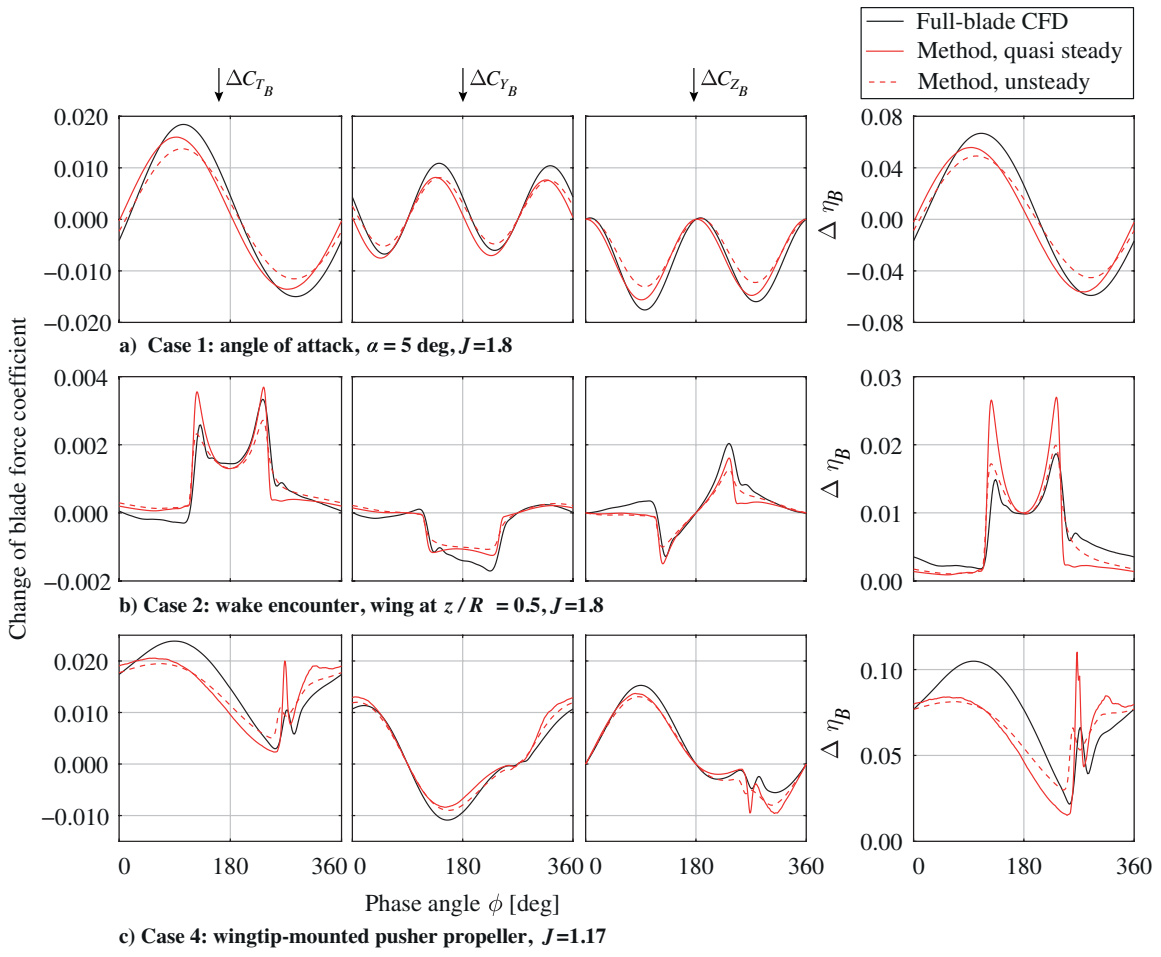

Fig. 12 Comparison of the change of the integral blade forces predicted by the method and computed by means of full-blade CFD simulations.

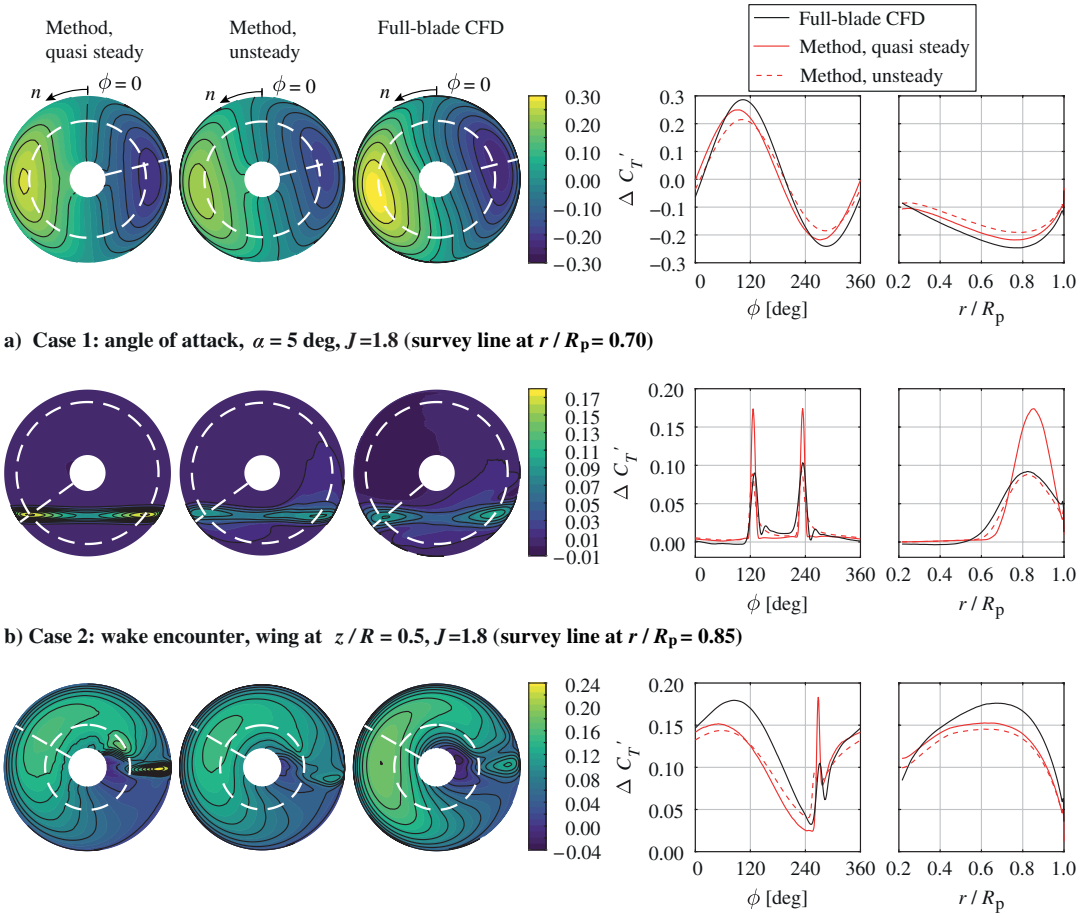

a) Case 1: angle of attack, $\alpha = 5$ deg, $J = 1.8$ (survey line at $r / R_p = 0.70$)

b) Case 2: wake encounter, wing at $z / R = 0.5$, $J = 1.8$ (survey line at $r / R_p = 0.85$)

c) Case 4: wingtip-mounted pusher propeller, $J = 1.17$ (survey line at $r / R_p = 0.50$)

Fig. 13 Comparison of the predicted change of the propeller thrust distribution with full-blade CFD results. The local thrust coefficient along the dashed lines is shown on the right.

in radial direction, the unsteady method already shows excellent agreement of the radial load distribution for a range of phase angles. The integral forces depicted in Fig. 14b are close to the ones computed in the full-blade simulation; in particular, the changes in thrust and torque are well predicted. The relative changes of the thrust and torque are also in line with the full-blade CFD simulations, which are reflected in the change in blade efficiency (Fig. 12b).

Case 4 exhibits comparable trends as in validation cases 1 and 2 in terms of integral blade forces if the quasi-steady method is used, as depicted in Fig. 12c. First, there is a local overprediction in the regions of a local disturbance induced by the wing wake; second, there is an underprediction of the effect introduced by a distributed nonuniformity over the disk, i.e., the swirling inflow; and finally, there is a phase advance with respect to the full-blade simulation. Similar to the previously discussed cases, the contour plot in Fig. 13c reveals that the shape of the thrust distribution is very well captured by the method, despite the overpredictions in the regions where there is a strong gradient of the inflow: the encounter of the wing wake and the impingement of the wingtip vortex. In a qualitative manner, one can directly relate the relative importance of the different flow phenomena on the propeller loads by relating the thrust distribution to the inflow field of Fig. 11d. Figure 14d shows that the integral thrust is close to the computed value of the full-blade CFD simulation, and the order of magnitude and direction of the in-plane forces is correctly captured. Quantitatively, the in-plane forces of this case are relatively small, and a difference in phase quickly causes a relatively large offset.

Finally, for case 3, the large reduction in the thrust observable in Fig. 14c is caused by the higher axial inflow velocity induced by the wing's circulation. When the tip clearance is increased, the reduction in thrust becomes smaller. With increasing tip clearance, the wing's influence on the propeller reduces, and this trend is very well predicted by the method, despite the complex flowfield and the proximity of the propeller and wing. Additionally, the predicted magnitude of the ΔC_T almost coincides with the measured values, and it shows the ability of the method to predict the propeller performance for such configuration. The model is also able to capture the different response of the propeller thrust coefficient to the nonuniform inflow for each advance ratio because the sensitivity to a change in advance ratio depends on the nominal operating condition.

For the cases evaluated, it was found that the change of the integral thrust and torque compared to the uniform inflow condition were within a range of 0.5 to 12% compared to the validation data. It is concluded that the method is able to capture the relevant changes in propeller loading, and it can predict both the magnitude and trends well for a wide range of operating conditions and nonuniform inflows.

C. Computational Efficiency Benefits of the Method

The computational cost of a single condition using the engineering method was found to be on the order of several seconds, whereas a significant amount of computational efforts was spent on the unsteady full-blade CFD simulations to evaluate a single operating condition, as listed in Table 5. The additional time to correct the quasi-steady results for unsteady effects is negligible. If one is only interested in the change in integral thrust or torque, the unsteady correction is even redundant. The construction of the performance maps in Fig. 10 required approximately 2000 CPU hours, whereas it is noted that the large number of conditions (20 advance ratios) could be reduced to a minimum of two conditions in case the nonlinear regime is not of interest. The values in Table 5 clearly demonstrate the advantage of using the engineering method for an initial estimate of the propeller performance as well as the phase-accurate blade responses: in

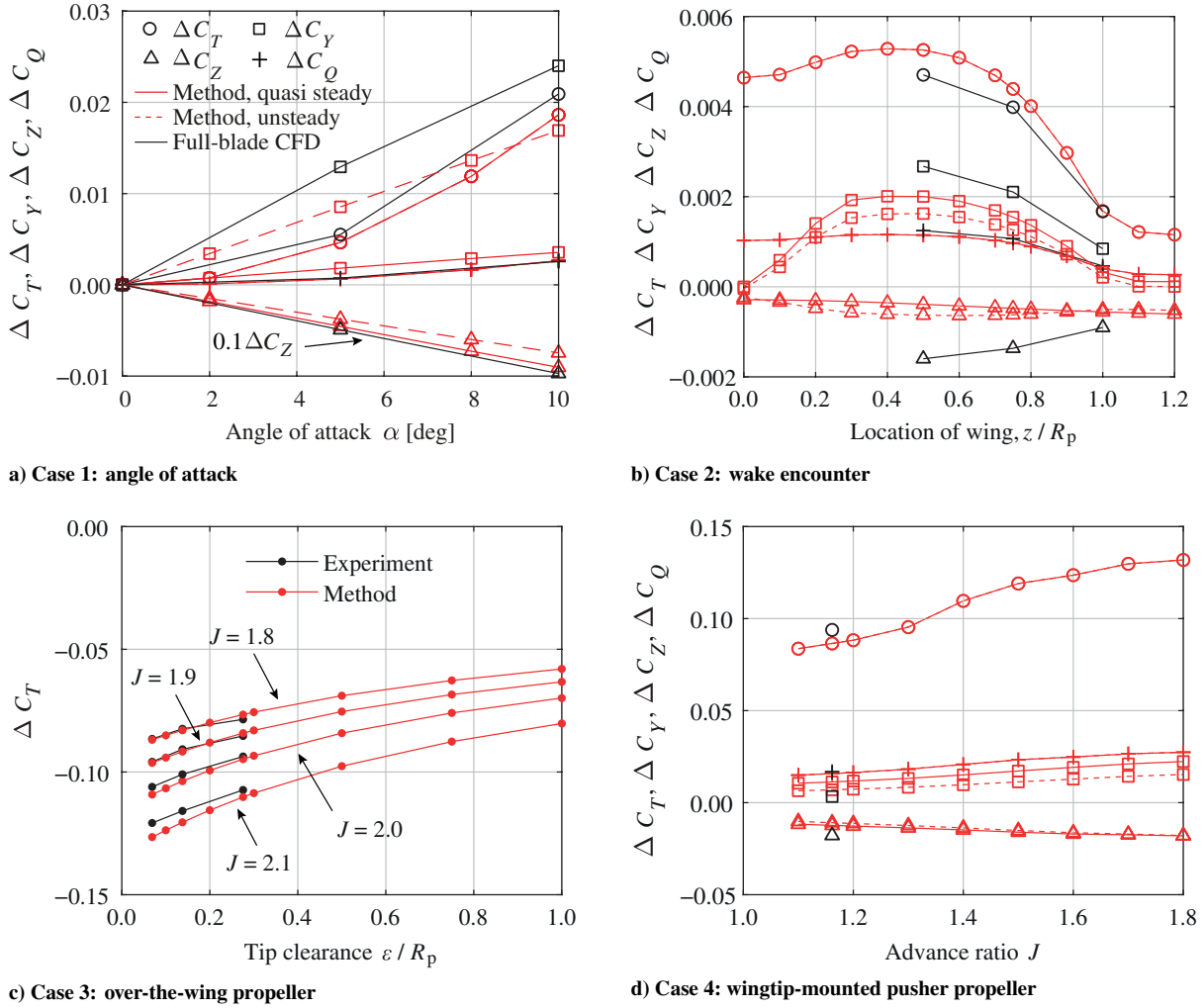

a) Case 1: angle of attack

b) Case 2: wake encounter

c) Case 3: over-the-wing propeller

d) Case 4: wingtip-mounted pusher propeller

Fig. 14 Comparison of the change of the integral propeller forces as predicted by the method and validation data from full-blade CFD simulations and wind-tunnel tests.

Table 5 Comparison of computational efforts of engineering method to full-blade CFD

Case no.	Characterization C_T–J, CPU hours	Simulate inflow, CPU hours	Single condition method, CPU seconds	Single condition full-blade CFD, CPU hours
1	~2000	160	~3	7000
2	~2000	180	~3	7500
4	~1900	210	~4	8500

particular, if a large number of conditions are to be evaluated. This makes the proposed method highly valuable for the design of vehicles with tightly integrated propellers.

V. Conclusions

This paper has presented an engineering method to estimate the propeller load distribution for propellers operating in arbitrary nonuniform flow. The method is computationally extremely efficient because the input is based on the distribution of the thrust and torque along the propeller radius to a change in advance ratio for the uninstalled propeller in uniform inflow. It is shown that the shape of the sensitivity distributions is nearly independent of the propeller advance ratio, and it can therefore be approximated by simulating only two operating conditions. The construction of these sensitivity distributions also provides insight into what region of the disk leads to the largest response in propeller forces; this was demonstrated to be the region of highest loading.

The method was applied to four representative validation cases: a propeller at an angle of attack, a propeller encountering a wake, an over-the-wing propeller, and a wingtip-mounted pusher propeller. A phase difference with respect to full-blade CFD simulations is present in the case of a distributed disturbance, leading to slight inaccuracy of the prediction of the in-plane forces. The application of a correction on the quasi-steady results nearly removes the difference in phase between the responses of the validation data and the method, and it improves the difference in magnitude of the blade response as the result of local disturbances in inflow. The integral forces on the individual blades over a full revolution as well as the integral propeller forces compare well with the validation data: both in terms of predicted trends and magnitude. For the evaluated cases, it is shown that the change in the load due to the nonuniform inflow is predicted with errors ranging from 0.5 up to 12% compared to the validation data.

The acceptable agreement with full-blade simulations and experimental results also demonstrates that, for most configurations, the

dominating factor to alter the propeller performance is the flowfield induced by the airframe in the absence of the propeller. The method has been applied for slender blades, represented as a line through the midchord.

The proposed method offers significant efficiency benefits over conventional unsteady CFD analyses of installed propeller. The unsteady analyses of the full annulus of the installed propeller are avoided, whereas a time-resolved solution is still obtained, with a temporal resolution depending on the spatial resolution of the inputs. The proposed method provided a time-resolved solution within several CPU seconds, which was seven orders of magnitude faster than with the full-blade RANS CFD computations. The low computational cost makes the proposed method suitable for both the design and analyses of propellers in arbitrary nonuniform flows. Compared to relying on isolated performance data, this method will allow for a better prediction of the performance of aircraft with tightly integrated propellers, as well as an estimation of the propeller contribution to the aircraft stability derivatives during the preliminary design phase.

Acknowledgments

The project leading to these results has received funding from the Clean Sky 2 Joint Undertaking under the European Union's Clean Sky 2 Large Passenger Aircraft program (CS2-LPA-GAM-2018-2019-01). The authors would like to thank Tom Stokkermans for providing the geometry and setup of the wingtip-mounted pusher-propeller simulation.

References

[1] Goldsmith, I. M., "A Study to Define the Research and Technology Requirements for Advanced Turbo/Propfan Transport Aircraft," NASA CR-166138, 1981.

[2] Miley, S. J., and von Lavante, E., "Propeller Propulsion System Integration State of Technology Survey," NASA CR-3882, 1985.

[3] Hager, R. D., and Vrabel, D., "Advanced Turboprop Project," NASA SP-495, 1988.

[4] Whitlow, J. B., and Sievers, G. K., "Fuel Savings Potential of the NASA Advanced Turboprop Program," NASA TM-83736, 1984.

[5] Yaros, S. F., Sexstone, M. G., Huebner, L. D., Lamar, J. E., McKinley, R. E., Jr., Torres, A. O., Burley, C. L., Scott, R. C., and Small, W. J., "Synergistic Airframe-Propulsion Interactions and Integrations," NASA TM-1998-207644, 1998.

[6] Janus, J. M., Chatterjee, A., and Cave, C., "Computational Analysis of a Wingtip-Mounted Pusher Turboprop," *Journal of Aircraft*, Vol. 33, No. 2, 1996, pp. 441–444. https://doi.org/10.2514/3.46959

[7] Snyder, M. H., Jr., and Zumwalt, G. W., "Effects of Wingtip-Mounted Propellers on Wing Lift and Induced Drag," *Journal of Aircraft*, Vol. 6, No. 5, 1969, pp. 392–397. https://doi.org/10.2514/3.44076

[8] Miranda, L. R., and Brennan, J. E., "Aerodynamic Effects of Wingtip-Mounted Propellers and Turbines," *AIAA 4th Applied Aerodynamics Conference*, AIAA Paper 1986-1802, 1986. https://doi.org/10.2514/6.1986-1802

[9] Patterson, J. C., Jr., and Bartlett, G. R., "Evaluation of Installed Performance of a Wing-Tip-Mounted Pusher Turboprop on a Semispan Wing," NASA TP-2739, 1978.

[10] Kroo, I., "Propeller/Wing Integration for Minimum Induced Loss," *Journal of Aircraft*, Vol. 23, No. 7, 1986, pp. 561–565. https://doi.org/10.2514/3.45344

[11] Sinnige, T., van Arnhem, N., Stokkermans, T. C. A., Eitelberg, G., and Veldhuis, L. L. M., "Wingtip-Mounted Propellers: Aerodynamic Analysis of Interaction Effects and Comparison with Conventional Layout," *Journal of Aircraft*, Vol. 56, No. 1, 2019, pp. 295–312. https://doi.org/10.2514/1.C034978

[12] Johnson, J. L., and White, E. R., "Exploratory Low-Speed Wind-Tunnel Investigation of Advanced Commuter Configurations Including an Over-the-Wing Propeller Design," *AIAA Aircraft Design, Systems and Technology Meeting*, AIAA Paper 1983-2531, 1983. https://doi.org/10.2514/6.1983-2531

[13] Müller, L., Heinze, W., Kožulović, D., Hepperle, M., and Radespiel, R., "Aerodynamic Installation Effects of an Over-the-Wing Propeller on a High-Lift Configuration," *Journal of Aircraft*, Vol. 51, No. 1, 2014, pp. 249–258. https://doi.org/10.2514/1.C032307

[14] Veldhuis, L. L. M., and Khajehzadeh, A., "Analysis and Design of a Wing Trailing Edge Mounted Over-the-Wing Distributed Propeller Propulsion System," *AIAA Aviation Forum*, AIAA Paper 2019-3692, 2019. https://doi.org/10.2514/6.2019-3692

[15] Marcus, E. A. P., de Vries, R., Raju Kulkarni, A., and Veldhuis, L. L. M., "Aerodynamic Investigation of an Over-the-Wing Propeller for Distributed Propulsion," *AIAA SciTech Forum*, AIAA Paper 2018-2053, 2018. https://doi.org/10.2514/6.2018-2053

[16] de Vries, R., van Arnhem, N., Avallone, F., Ragni, D., Vos, R., Eitelberg, G., and Veldhuis, L. L. M., "Aerodynamic Interaction Between an Over-the-Wing Propeller and the Wing Boundary-Layer in Adverse Pressure Gradients," *AIAA Aviation Forum*, AIAA Paper 2019-3035, 2019. https://doi.org/10.2514/6.2019-3035

[17] Lv, P., Rao, A. G., Ragni, D., and Veldhuis, L. L. M., "Performance Analysis of Wake and Boundary-Layer Ingestion for Aircraft Design," *Journal of Aircraft*, Vol. 53, No. 5, 2016, pp. 1517–1526. https://doi.org/10.2514/1.C033395

[18] Seitz, A., and Gologan, C., "Parametric Design Studies for Propulsive Fuselage Aircraft Concepts," *CEAS Aeronautical Journal*, Vol. 6, No. 1, 2015, pp. 69–82. https://doi.org/10.1007/s13272-014-0130-3

[19] Borer, N. K., Patterson, M. D., Viken, J. K., Moore, M. D., Bevirt, J., Stoll, A. M., and Gibson, A. R., "Design and Performance of the NASA SCEPTOR Distributed Electric Propulsion Flight Demonstrator," *16th AIAA Aviation Technology, Integration, and Operations Conference, AIAA AVIATION Forum*, AIAA Paper 2016-3920, 2016. https://doi.org/10.2514/6.2016-3920

[20] de Vries, R., Hoogreef, M. F. M., and Vos, R., "Aeropropulsive Efficiency Requirements for Turboelectric Transport Aircraft," *AIAA SciTech Forum*, AIAA Paper 2020-0502, 2020. https://doi.org/10.2514/6.2020-0502

[21] Durand, W., *Aerodynamic Theory*, Vol. IV, Springer, New York, 1935, pp. 251–254, 269–292.

[22] Nallasamy, M., "Unsteady Blade Pressures on a Propfan: Predicted and Measured Compressibility Effects," *AIAA Joint Propulsion Conference*, AIAA Paper 1992-3774, 1992. https://doi.org/10.2514/6.1992-3774

[23] Heidelberg, L. J., and Nallasamy, M., "Unsteady Blade Pressure Measurements for the SR-7A Propeller at Cruise Conditions," *AIAA Aeroacoustics Conference*, AIAA Paper 1990-4022, 1990. https://doi.org/10.2514/6.1990-4022

[24] Janus, J. M., "General Aviation Propeller-Airframe Integration Simulations," *Journal of Aircraft*, Vol. 43, No. 2, 2006, pp. 390–394. https://doi.org/10.2514/1.15354

[25] de Young, J., "Propellers at High Incidence," *Journal of Aircraft*, Vol. 2, No. 3, 1965, pp. 241–250. https://doi.org/10.2514/3.43646

[26] Applin, Z. T., and Coe, P. L., Jr., "Low-Speed Stability and Control Characteristics of a Transport Model with Aft-Fuselage-Mounted Advanced Turboprops," NASA TP 2535, 1986.

[27] van Arnhem, N., de Vries, R., Vos, R., and Veldhuis, L. L. M., "Aerodynamic Performance of an Aircraft Equipped with Horizontal Tail-Mounted Propellers," *AIAA Aviation Forum*, AIAA Paper 2019-3036, 2019. https://doi.org/10.2514/6.2019-3036

[28] Obert, E., *A Method for the Determination of the Effect of Propeller Slipstream on the Static Longitudinal Stability and Control of Multi-Engined Aircraft*, Delft Univ. Press, Delft, The Netherlands, 1997, p. 13.

[29] Yang, Y., Zhou, T., Sciacchitano, A., Veldhuis, L., and Eitelberg, G., "Propeller and Inflow Vortex Interaction: Vortex Response and Impact on the Propeller Performance," *CEAS Aeronautical Journal*, Vol. 7, No. 3, 2016, pp. 419–428. https://doi.org/10.1007/s13272-016-0198-z

[30] Sinnige, T., Ragni, D., Malgoezar, A. M. N., Eitelberg, G., and Veldhuis, L. M. M., "APIAN-INF: An Aerodynamic and Aeroacoustic Investigation of Pylon-Interaction Effects for Pusher Propellers," *CEAS Aeronautical Journal*, Vol. 9, No. 2, 2018, pp. 291–306. https://doi.org/10.1007/s13272-017-0247-2

[31] Sinnige, T., Ragni, D., Eitelberg, G., and Veldhuis, L. M. M., "Mitigation of Pusher-Propeller Installation Effects by Pylon Trailing-Edge Blowing," *Journal of Aircraft*, Vol. 54, No. 1, 2017, pp. 292–300. https://doi.org/10.2514/1.C034000

[32] Block, P. J. W., and Gentry, G. L., Jr., "Directivity and Trends of Noise Generated by a Propeller in a Wake," NASA TP 2609, 1986.

[33] Bushnell, P., Gruber, M., and Parzyck, D., "Measurement of Unsteady Blade Surface Pressures on a Single Rotation Large-Scale Advanced Propfan with Angular and Wake Inflow at Mach Numbers from 0.02 to 0.70," NASA CR 182123, 1988.

[34] Neuwerth, G., Lölgen, T., and Staufenbiel, R., "Increased Noise Emission of Propellers and Propfans due to Pusher Installation," *17th ICAS Congress Proceedings*, Vol. 1, ICAS, 1990, pp. 127–138.
[35] Gérard, A., Berry, A., Masson, P., and Gervais, Y., "Evaluation of Tonal Aeroacoustic Sources in Subsonic Fans Using Inverse Models," *AIAA Journal*, Vol. 45, No. 1, 2007, pp. 98–109. https://doi.org/10.2514/1.21957
[36] Ruiz-Calavera, L. P., and Perdones-Diaz, D., "CFD Computation of In-Plane Propeller Shaft Loads," *AIAA/ASME/SAE/ASEE Joint Propulsion Conference*, AIAA Paper 2013-3798, 2013. https://doi.org/10.2514/6.2013-3798
[37] Nallasamy, M., and Groeneweg, J. F., "Unsteady Euler Analysis of the Flow Field of a Propfan at an Angle of Attack," NASA TM 102426, 1990.
[38] Ortun, B., Boisard, R., and Gonzalez-Martino, I., "In-Plane Airloads of a Propeller with Inflow Angle: Prediction vs. Experiment," *30th Applied Aerodynamics Conference*, AIAA Paper 2012-2778, 2012. https://doi.org/10.2514/6.2012-2778
[39] Stuermer, A. W., "Unsteady CFD Simulations of Propeller Installation Effects," *AIAA Joint Propulsion Conference*, AIAA Paper 2006-4969, 2006. https://doi.org/10.2514/6.2006-4969
[40] Veldhuis, L. L. M., van Berkel, E., Kotsonis, M., and Eitelberg, G., "Non-Uniform Inflow Effects on Propeller Performance," *AIAA Applied Aerodynamics Conference*, AIAA Paper 2013-2801, 2013. https://doi.org/10.2514/6.2013-2801
[41] Sinnige, T., van Arnhem, N., Stokkermans, T. C. A., Eitelberg, G., and Veldhuis, L. L. M., "Wingtip-Mounted Propellers: Aerodynamic Analysis of Interaction Effects and Comparison with Conventional Layout," *Journal of Aircraft*, Vol. 56, No. 1, 2019, pp. 295–312. https://doi.org/10.2514/1.C034978
[42] van Arnhem, N., Sinnige, T., Stokkermans, T. C. A., Eitelberg, G., and Veldhuis, L. L. M., "Aerodynamic Interaction Effects of Tip-Mounted Propellers Installed on the Horizontal Tailplane," *AIAA Aerospace Sciences Meeting*, AIAA Paper 2018-0542, 2018. https://doi.org/10.2514/6.2018-0542
[43] Stokkermans, T. C. A., van Arnhem, N., and Veldhuis, L. L. M., "Mitigation of Propeller Kinetic Energy Losses with Boundary Layer Ingestion and Swirl Recovery Vanes," *Applied Aerodynamics Conference*, RAeS, 2016.
[44] Stokkermans, T. C. A., Nootebos, S., and Veldhuis, L. L. M., "Analysis and Design of a Small-Scale Wingtip-Mounted Pusher Propeller," *AIAA Aviation Forum*, AIAA Paper 2019-3693, 2019. https://doi.org/10.2514/6.2019-3693
[45] Stokkermans, T. C. A., Voskuijl, M., Veldhuis, L. L. M., Soemarwoto, B., Fukari, R., and Eglin, P., "Aerodynamic Installation Effects of Lateral Rotors on a Novel Compound Helicopter Configuration," AHS International, 2018.
[46] Schulten, J. B. H. M., "Advanced Propeller Performance Calculation by a Lifting Surface Method," *Journal of Propulsion and Power*, Vol. 12, No. 3, 1996, pp. 477–485. https://doi.org/10.2514/3.24060
[47] Hanson, D. B., "Compressible Lifting Surface Theory for Propeller Performance Calculation," *Journal of Aircraft*, Vol. 22, No. 1, 1985, pp. 19–27. https://doi.org/10.2514/3.45075
[48] Gur, O., and Rosen, A., "Comparison Between Blade-Element Models of Propellers," *Aeronautical Journal*, Vol. 112, No. 1138, 2008, pp. 689–704. https://doi.org/10.1017/S0001924000002669
[49] Boctor, M. L., Clay, C. W., and Watson, C. F., "An Analysis of Prop-Fan Airframe Aerodynamic Integration," NASA CR 152186, 1978.
[50] Veldhuis, L. L. M., "Propeller Wing Aerodynamic Interference," Ph.D. Thesis, Delft Univ. of Technology, Delft, The Netherlands, 2005.
[51] Ragni, D., van Oudheusden, B. W., and Scarano, F., "Stereoscopic Particle Image Velocimetry-Based Integral Load Determination on an Aircraft Propeller," *Journal of Aircraft*, Vol. 49, No. 5, 2012, pp. 1497–1506. https://doi.org/10.2514/1.C031853
[52] Schetz, J. A., Mallory, D. A., and Pelletier, D., "Numerical and Experimental Investigation of a Propeller Flowfield with a 3-D Non-Uniform Inflow," *25th Aerospace Sciences Meeting*, AIAA Paper 1987-0607, 1987. https://doi.org/10.2514/6.1987-607
[53] "Prediction of Near-Field and Far-Field Harmonic Noise from Subsonic Propellers with Non-Axial Inflow," Engineering Sciences Data Unit TR ESDU 11005, London, 2018.
[54] Finck, R., *USAF (United States Air Force) Stability and Control DATCOM (Data Compendium)*, McDonnell Aircraft, St. Louis, MO, 1978. https://doi.org/10.21236/adb072483
[55] Stokkermans, T. C. A., van Arnhem, N., Sinnige, T., and Veldhuis, L. L. M., "Validation and Comparison of RANS Propeller Modeling Methods for Tip-Mounted Applications," *AIAA Journal*, Vol. 57, No. 2, 2019, pp. 566–580. https://doi.org/10.2514/1.J057398
[56] Whitfield, D. L., Swafford, T. W., Janus, J. M., Mulac, R.A., and Belk, D. M., "Three Dimensional Unsteady Euler Solutions for Propfans and Counter-Rotating Propfans," *AIAA 19th Fluid Dynamics, Plasma Dynamics and Lasers Conference*, AIAA Paper 1987-1197, 1987. https://doi.org/10.2514/6.1987-1197
[57] Succi, G. P., "Design of Quiet Efficient Propellers," *SAE Transactions*, Vol. 88, Jan. 1979, pp. 2039–2052.
[58] Allen, C. S., and Korkan, K. D., "Influence of a Non-Uniform Free Stream Velocity Distribution on Performance/Acoustics of Counter-rotating Propeller Configurations," *29th Aerospace Sciences Meeting*, AIAA Paper 1991-0195, 1991. https://doi.org/10.2514/6.1991-195
[59] Martinez, R., "Predictions of Wing and Pylon Forces Caused by Propeller Installation," NASA CR-178298, 1987.
[60] von Karman, T., and Sears, W. R., "Airfoil Theory for Non-Uniform Motion," *Journal of Aeronautical Sciences*, Vol. 5, No. 10, 1938, pp. 379–390. https://doi.org/10.2514/8.674
[61] Sears, W. R., "Some Aspects of Non-Stationary Airfoil Theory and Its Practical Application," *Journal of the Aeronautical Sciences*, Vol. 8, No. 3, 1941, pp. 104–108. https://doi.org/10.2514/8.10655
[62] Amiet, R. K., "Compressibility Effects in Unsteady Thin-Airfoil Theory," *AIAA Journal*, Vol. 12, No. 2, 1974, pp. 252–255. https://doi.org/10.2514/3.49212
[63] McCune, J. E., "Unsteady Wing Theory—The Kármán/Sears Legacy," *1st National Fluid Dynamics Conference*, AIAA Paper 1988-3539, 1988. https://doi.org/10.2514/6.1988-3539
[64] Simpson, R. J. S., Palacios, R., and Murua, J., "Induced-Drag Calculations in the Unsteady Vortex Lattice Method," *AIAA Journal*, Vol. 51, No. 7, 2013, pp. 1775–1779. https://doi.org/10.2514/1.J052136
[65] Li, Q., Öztürk, K., Sinnige, T., Ragni, D., Eitelberg, G., Veldhuis, L. L. M., and Wang, Y., "Design and Experimental Validation of Swirl-Recovery Vanes for Propeller Propulsion Systems," *AIAA Journal*, Vol. 56, No. 12, 2018, pp. 4719–4729. https://doi.org/10.2514/1.J057113
[66] "ANSYS® Fluent User's Guide," Release 18.1, Sec. 10.3, ANSYS Inc.
[67] Spalart, P. R., and Rumsey, C. L., "Effective Inflow Conditions for Turbulence Models in Aerodynamic Calculations," *AIAA Journal*, Vol. 45, No. 10, 2007, pp. 2544–2553. https://doi.org/10.2514/1.29373.
[68] Eça, L., and Hoekstra, M., "Discretization Uncertainty Estimation Based on a Least Squares Version of the Grid Convergence Index," *Proceedings of the Second Workshop on CFD Uncertainty Analysis*, 2006.
[69] Ewald, B., "Wind Tunnel Wall Corrections," Advisory Group for Aerospace Research and Development TR AGARD-AG-336, Neuilly-Sur-Seine, France, 1998.
[70] Gracey, W., Letko, W., and Russel, W. R., "Wind-Tunnel Investigation of a Number of Total-Pressure Tubes at High Angles of Attack," NACA TN 2331, 1951.
[71] Westerweel, J., "Fundamentals of Digital Particle Image Velocimetry," *Measurement Science and Technology*, Vol. 8, No. 12, 1997, pp. 1379–1392. https://doi.org/10.1088/0957-0233/8/12/002
[72] Bass, R. M., "Small Scale Wind Tunnel Testing of Model Propellers," *AIAA 24th Aerospace Sciences Meeting*, AIAA Paper 1986-392, 1986. https://doi.org/10.2514/6.1986-392
[73] Schülein, E., Rosemann, H., and Schaber, S., "Transition Detection and Skin Friction Measurements on Rotating Propeller Blades," *Aerodynamic Measurement Technology, Ground Testing, and Flight Testing Conference*, AIAA Paper 2012-3202, 2012. https://doi.org/10.2514/6.2012-3202
[74] van Arnhem, N., Vos, R., and Veldhuis, L. L. M., "Aerodynamic Loads on an Aft-Mounted Propeller Induced by the Wing," *AIAA Aerospace Sciences Meeting*, AIAA Paper 2019-1093, 2019. https://doi.org/10.2514/6.2019-1093

F. N. Coton
Associate Editor